Chapter 3
Neutron Scattering Instrumentation

Helmut Schober

Abstract This chapter gives a short introduction into neutron scattering instrumentation to allow the non-specialist reader to acquire the basics of the method necessary to understand the technical aspects in the topical articles. The idea is not to go into details but to elaborate on the principles as general as possible. We start with a short discussion of neutron production at large-scale facilities. We then present the main characteristics of neutron beams and show how these can be tailored to the specific requirements of the experiment using neutron optical devices and time-of-flight discrimination. This will allow us in the final section to present a non-exhaustive selection of instrument classes. Emphasis will be given to the design aspects responsible for resolution and dynamic range, as these define the field of scientific application of the spectrometers.

3.1 Introduction

Free neutrons are elementary particles discovered by James Chadwick [1, 2] in 1932. The quantum mechanical state of a free neutron is determined by the momentum $|\vec{p}>$ ($\vec{p} = \hbar\vec{k}, k = h/\lambda$) and spin state $|s>$, where, for all practical purposes, it will be sufficient to work with non-relativistic energies ($E = \hbar^2k^2/2m$). The mass of the neutron[1] is given as 1.008 amu, which leads us to the relation between energy and wavelength of a neutron:

$$E[\text{meV}] \equiv 2.0725k^2\left[\text{Å}^{-2}\right] \equiv 81.8204\lambda^{-2}\left[\text{Å}^{2}\right]. \tag{3.1}$$

[1]We use the constants as given by the National Institute of Standards and Technology (http://physics.nist.gov/cuu/Constants/): $h = 6.62606896 \times 10^{-34}$ Js and $m = 1.674927211 \times 10^{-27}$ kg. As $e = 1.602176487 \times 10^{-19}$ C, one Joule is equivalent to $6.24150965 \times 10^{18}$ eV. A wealth of interesting information on neutron and on neutron instrumentation can be found in the Neutron Data Booklet [3].

H. Schober (✉)
Institut Laue-Langevin, F-38042 Grenoble, France
e-mail:Schober@ill.fr

L. Liang et al. (eds.), *Neutron Applications in Earth, Energy and Environmental Sciences*, Neutron Scattering Applications and Techniques,
DOI 10.1007/978-0-387-09416-8_3,

The spin of the neutron is $1/2$ with an associated magnetic moment μ_n of -1.9132 nuclear magnetons. A more detailed discussion of the spin properties is given in the section on spin - echo spectroscopy.

Neutrons interact with the nuclei of the sample via the strong interaction and with the electrons via their magnetic dipole moment. In both cases the scattering is weak for thermal and cold neutrons. Neutrons thus constitute a simple, non-destructive probe of matter. As neutrons penetrate deeply into matter, it is rather straightforward to use even complex and bulky sample environments. This fortunately does not prevent neutrons from being highly sensitive, which is capable of investigating minority components of a sample down to a few ppm. Neutrons are equally very well suited to the study of films and interfaces of atomic thickness.

To profit fully from these extraordinary analytic capacities, tentatively summarized in Table 3.1, requires optimized instrumentation. This is the more important as even at the strongest sources neutron scattering remains a flux-limited technique. It is the aim of this chapter to outline the principles of neutron production and neutron instrumentation. It is one of our main objectives to demonstrate how by profiting from modern technology it is possible to considerably improve the performance of both neutron sources and instruments.

The philosophy underlying this chapter is to discuss instruments in terms of functional building blocks. From this functional point of view, a monochromator or a time-of-flight chopper cascade are quite similar as both constitute filters that slice wavelength bands from the beam. Speaking in more general terms, instrument devices reshape the phase space elements that describe what kind of neutrons are present with what probability at any time t and at any place $\vec{r}$ along the beam trajectory. Optical elements, for example, reshape phase space elements by concentrating the beam intensity in space or by rendering the beam more parallel. It is the transformation of phase space elements that fully characterizes the performance of a single device. When assembling building blocks to create an instrument, it is important to realize that the phase space element shaped by one component constitutes the raw material for the subsequent transformation stage. The whole instrument can, therefore, be viewed as a production line with the individual instrument components shaping and consecutively transferring the beam. In this approach the sample is just

Table 3.1 Present performance parameters of neutron scattering instrumentation. The values are to be taken as indicative. In an actual experiment the specificities of the sample and the exact nature of the scientific question are decisive

In space	In time
Sample volume for structure studies: 10^{-3} mm^3	Shortest oscillation periods: 10^{-15} s
Mass for dynamic studies: 5 mg (protonated), 50 mg (other)	Longest observable relaxation time: 1 μs
Maximum accuracy in distances: 10^{-3} nm	Maximum resolution in real time: 0.1 ms
Largest observable object size: 0.1 mm	Stability in time: years
Chemical sensitivity 10 ppm	
Magnetic sensitivity $0.01\mu_B$ / atom	
Accuracy on direction of magnetic moment: 0.5°	

one of the many components that make up the instrument.[2] Its beam shaping and beam transfer capacities are described by the double differential scattering cross section or scattering law. Determining this scattering law with high precision is the whole purpose of the experiment. It is evident that there has to be a perfect match of device characteristics to achieve this goal in an efficient manner. As we hopefully will be able to demonstrate, optimizing and matching phase space elements are the whole art of instrument design.

3.2 Neutron Sources

While neutrons are omnipresent in the universe, they are very rare in the free state. Most of them are actually bound in nuclei or neutron stars. We, therefore, have to free the neutrons from the nuclei via technological processes like fission or spallation. Once produced, free neutrons do not live forever, but have a limited lifetime of about 886 seconds.

3.2.1 Method of Production

A good neutron source produces a high density of neutrons of appropriate wavelength and time structure. It is essential that the neutrons can be extracted from the source and transported efficiently to the spectrometers. This requires a two-stage process. First, neutrons bound in nuclei are liberated via nuclear excitation and subsequent nuclear decay processes. Due to the energies involved in these nuclear reactions (several MeV), this produces high-energy, that is, very short wavelength neutrons that are not well suited for the purpose of investigating condensed matter on the nanometer length scale (a few meV). The necessary slowing down of the neutrons is achieved in a second stage via *moderation*, that is, scattering of the neutrons by the moderator atoms or molecules.

There are many nuclear reactions that count neutrons among their final products. The yield is, however, in most cases insufficient for neutron scattering applications. Today, there are only two processes in use that extract a sufficient number of neutrons from nuclei: fission and spallation. Recently, laser-induced fusion was proposed as an alternative way of neutron production [4]. As controlled and sustained fusion involves a high degree of technical complexity, this concept would, however, reach maturity and applicability only after decades of development.

In the case of *fission*, slow neutrons are absorbed by metastable ^{235}U. The excited nucleus decays in a cascade of fission products. On the average 2.5 neutrons are produced by the fission of one ^{235}U nucleus. These neutrons possess very elevated

[2] Bragg scattering from a sample provides the necessary information about its atomic structure. If the same Bragg reflection is used for monochromating the beam, then the sample becomes a technical instrumental device.

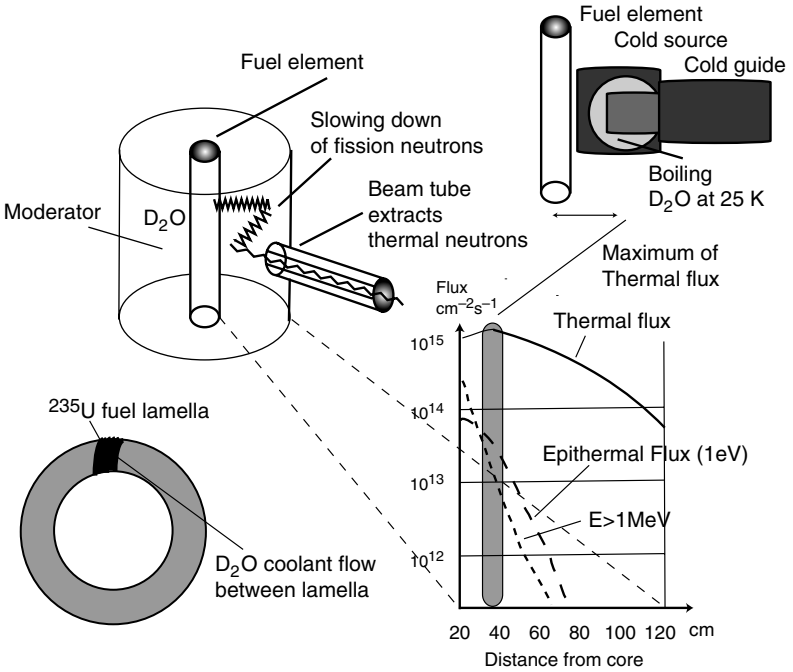

Fig. 3.1 Schematics of the ILL research reactor. A compact fuel element is surrounded by a D_2O moderator. Due to the collision with the D_2O molecules, the highly energetic neutrons from the ^{235}U fission are slowed down until they are in thermal equilibrium with the moderator. These processes produce a spectrum of thermal neutrons with a maximum in flux of 1.5×10^{15} neutrons per cm^2 per second, peaking at about 40 cm from the core center. Thermal beam tubes with noses placed close to the flux maximum extract these neutrons from the reactor core. One of these tubes feeds a suite of thermal neutron guides. In order to shift the neutron spectrum even further down in energy, two cavities with boiling D_2O are placed as close as technically possible to the thermal flux maximum. Cold neutron guides inserted into the beam tubes extract the spectrum from the cold source. A γ-heated graphite block (not shown) at 2400 K transposes the spectrum for certain beam tubes toward the higher energy end

energies of about 1 MeV and are unsuited for inducing further fission processes in ^{235}U. With the help of moderators, the fast neutrons are slowed down to meV energies (see Fig. 3.1). Light atoms are preferable as they take up an appreciable amount of the neutron energy at each collision. For H_2O we need about 18 collisions, while for the heavier D_2O 25 collisions are necessary.[3] These slow neutrons sustain the

[3] It is evident that the physics involved in moderation changes drastically along the cascade from MeV to meV. At high energies the collisions are inelastic, that is, they involve excitations of the nuclei that scatter the neutron. At low energies the equilibrium is attained via the exchange of low-frequency excitations of the moderator with the neutron. The character and spectrum of these excitations influence the moderation. In the case of H_2O and D_2O, the collisions involve, for example, predominantly rotational motions around the center of mass. This is the reason why it is the mass of H or D that counts for the moderation efficiency and not that of the molecule.

chain reaction in a nuclear reactor. By allowing some of the moderated neutrons to escape from the core region, free neutrons for scientific use are obtained. A high neutron density is achieved by using very compact core designs. A good moderator slows the neutrons down quickly. It creates a thermal flux that peaks at a short distance from the core, but far enough to allow for efficient beam extraction. The neutrons should have a long thermal diffusion length, that is, a long lifetime in the moderator. This precludes H_2O as a moderator material for very high-flux reactor neutron sources like the Institut Laue Langevin (ILL). Due to the absorption cross section of hydrogen, the thermal diffusion length of a neutron in H_2O is only about 3 cm while a mean free path of about 6 cm would be required for full moderation. In the case of D_2O, the thermal diffusion length is 1 m while full moderation is achieved within 10 cm.[4]

In the case of *spallation*, high-energy protons produced by an accelerator hit metallic targets like uranium, tungsten, lead, or mercury [5]. The thus excited nuclei "boil off" particles. Among these we encounter up to 20 high-energy neutrons.[5] As in the case of fission, the high-energy spallation neutrons have to be moderated to be useful for scattering applications. However, due to the different dimensions of the target, the size and shape of the moderators differ markedly from those used in reactors. The spallation process is about an order of magnitude more efficient than fission in producing neutrons; that is, a spallation source working with a 5 MW particle beam will produce about the same number of neutrons as a fission reactor of 50 MW thermal power. In terms of the overall energy balance, this is not a real advantage as the production of a 5 MW particle beam needs at least an order of magnitude higher electrical power.

3.2.2 Characteristics of the Source

In a standard reactor, neutrons are produced at a constant rate. The flux of neutrons thus has no explicit time structure. We are dealing with a *continuous* or *steady-state* neutron source. Typical examples of continuous neutron sources are the ILL reactor in Grenoble (see Fig. 3.1), France, the High-Flux Isotope Reactor (HFIR) at Oak Ridge National Laboratory (ORNL, Oak Ridge Tennessee), or the new Munich

[4] If the dimensions of the moderator are small, as in the case of a cold source, then H_2 may be a useful and easier - to - handle alternative to D_2 [6], despite the fact that D_2 would offer the optimum cold spectrum.

[5] The nuclear reactions following the impact of the proton beam depend on the proton energy. Below an excitation energy of 250 MeV, the boiling-off of neutrons is dominant. Most of them have energies in the 2 MeV range. This boiling-off is the main neutron production channel even for 1 GeV proton beams as normally only part of the proton energy is deposited in the target nuclei. There is, however, also an appreciable amount of faster neutrons. Their spectrum reaches up to the incident proton energy. These very fast neutrons require extremely heavy shielding around the target. The neutrons and the remaining excited nucleus engage in a cascade of secondary decay processes. Per useful neutron about 30 MeV of energy have to be evacuated in the case of spallation, compared to about 200 MeV in the case of fission.

reactor FRM-II in Germany. The unperturbed neutron thermal flux of the ILL is about 1.5×10^{15} neutrons $s^{-1}\,cm^{-2}$. Quasi-continuous neutron beams can equally be obtained via spallation. This is the case of the neutron source SINQ at the Paul Scherrer Institut (PSI) in Villigen, Switzerland.

In many cases it can be advantageous to work with pulsed neutron beams, as this allows the neutron energies to be determined by simply measuring the time of flight (see Section 3.3.6). At a continuous neutron source, this is achieved by the mechanical chopping devices incorporated into the spectrometer design. The production of pulsed neutron beams directly at the source is more or less straight forward in the case of spallation. It is sufficient to bunch the protons in the accelerator and storage ring. Depending on the time structure of the proton beam and the characteristics of the moderator, neutron pulses as short as a few microseconds can be produced at adapted rates of 50 or 60 Hz. This principle is used at *pulsed spallation sources* like ISIS in the UK, the SNS in the USA (see Fig. 3.2), or J-SNS in Japan.

It is important to keep the *incoherent nature* of all neutron sources in mind. Both production and moderation are accomplished via completely random events. Neutron sources thus have to be compared to light bulbs in optics. The lack of coherence, if translated into quantum mechanics, implies that there is no correlation of the phases of the neutron wave fields emanating from different regions of the source. Only the incoherent nature of the source makes it possible to describe the neutron beam by a probability distribution $p(\vec{k})$ in the wave-vector. For a coherent source like a LASER, the phase relation between different waves making up the wave field has to be taken into consideration.

As the moderation of the neutrons is done via collisions in a thermal bath (for example, D_2O, H_2, or D_2 molecules in the liquid state), the spectrum of the fully moderated neutrons can be considered a classical gas in thermal equilibrium and thus follows statistically a Maxwell–Boltzmann distribution governed by the temperature T of the bath.[6] The probability of finding a neutron in the state $|\vec{k}>$ is thus given by

$$p(\vec{k}) = \frac{1}{k_{\mathrm{T}}^3\sqrt{\pi^3}} \mathrm{e}^{-\frac{k^2}{k_{\mathrm{T}}^2}}, \tag{3.2}$$

with the mean neutron momentum and energy defined as

$$\hbar k_{\mathrm{T}} = \sqrt{2mk_{\mathrm{b}}T}, \qquad E_{\mathrm{T}} = \frac{1}{2m}\hbar^2 k_{\mathrm{T}}^2 = k_b T \tag{3.3}$$

and the Bolzmann constant

[6] In practice, the spectrum will differ from the ideal Maxwell–Boltzmann distribution. This is due to leakage of fast neutrons or incomplete moderation processes. These corrections become more important in the case of pulsed sources. The detailed shape of the source matters for the flux transmitted to the guides [7].

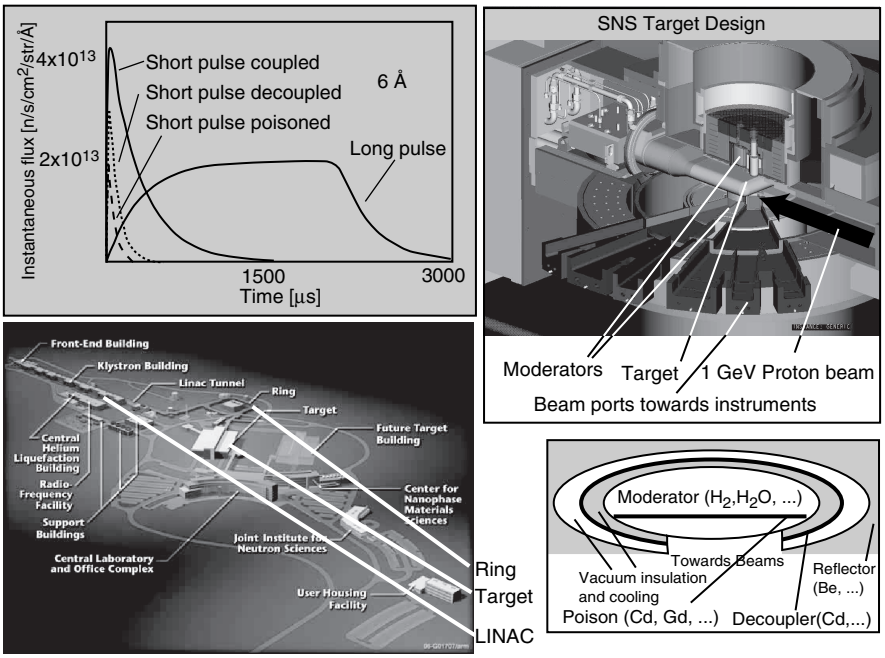

Fig. 3.2 Schematics of the SNS spallation source. H^- ions are produced by an ion source. The linac accelerates the H^- beam from 2.5 MeV to 1 GeV. The linac is a superposition of normal conducting and superconducting radiofrequency cavities that accelerate the beam and a magnetic lattice which provides focusing and steering. The H^- beam is stripped off its electrons, and the proton beam is compressed in a ring in time by about a factor 1000. After an accumulation of approximately 1200 turns, these protons are kicked out in a bunch, producing a microsecond pulse that is delivered to the liquid mercury target with a 60 Hz frequency. The high-energy neutrons coming out of the target are slowed down by passing them through cells filled with water (to produce room-temperature neutrons) or through containers of liquid hydrogen at a temperature of 20 K (to produce cold neutrons). These moderators are located above and below the target. The pulse shape depends strongly on the design of the moderator. Fully coupled moderators ensure that the neutrons get into full thermal equilibrium with the scattering medium. As this takes time, the corresponding pulses are long but the integrated intensity is high. Decoupled moderators give sharper pulses with less intensity. In the case of a poisoned decoupled moderator, neutrons that fall below a certain energy are confined to a layer at the moderator surface. This sharpens the pulse further. The basic principle of decoupling and poisoning a moderator is shown schematically in the lower right corner. The different pulse shapes as calculated for the ESS project [8, 9] are compared in the diagram. SNS is a short pulse spallation source. A long pulse source, as proposed for the next European source ESS, does not need an accumulator ring. Apart from the pulse shape, the repetition rate of the pulses is a crucial design parameter. The ratio of pulse length τ over pulse separation or repetition period T is called the duty cycle of the source. In the case of the SNS coupled moderator, it is about 2%. In principle, one would like to have very intense pulses at large intervals, that is, a low duty cycle. The lower limit on the repetition rate is set by the technological means required to produce more and more neutrons within a single pulse in order to maintain a maximum time averaged flux. These increase the cost and complexity of the accelerator and target. For example, at 8 Hz and 5 MW one would need 600 kJ/pulse, versus 23 kJ/pulse at SNS (60 Hz at 1.4 MW)

$$k_\mathrm{b} = 0.08617\,\mathrm{meV/K} \qquad \text{or} \qquad k_\mathrm{b}^{-1} = 11.60\,\mathrm{K/meV}. \tag{3.4}$$

The normalization is such that the integral over the phase space density

$$\mathrm{d}N = p(\vec{k})\mathrm{d}^3r\mathrm{d}^3k = \frac{N}{k_\mathrm{T}^3\sqrt{\pi^3}}\mathrm{e}^{-\frac{k^2}{k_\mathrm{T}^2}}\mathrm{d}^3r\mathrm{d}^3k \tag{3.5}$$

gives the total neutron density, which is assumed [10] to vary only slowly with $\vec{r}$. From the phase space density, we can calculate the energy distribution with

$$\Phi(E)\mathrm{d}E = \Phi_\mathrm{thermal}\frac{2}{\sqrt{\pi}}\frac{\sqrt{E}}{(k_\mathrm{b}T)^{3/2}}\exp\left(-\frac{E}{k_\mathrm{b}T}\right)\mathrm{d}E, \tag{3.6}$$

and

$$\Phi_\mathrm{thermal} = \frac{2N}{\sqrt{\pi}}v_\mathrm{T} = \frac{2N}{m\sqrt{\pi}}\hbar k_\mathrm{T}, \tag{3.7}$$

denoting the *thermal flux* of the source. Both at reactors and spallation sources, different moderators at different temperatures are used to give optimized flux distributions for the various scientific applications. At the ILL the thermal spectrum is moderated to lower energies by using boiling D_2 sources [7] at 25 K (see Fig. 3.1). The up-moderation is achieved via a graphite block heated to 2400 K via the γ-radiation.

At a short pulse source, the extremely narrow pulse of high-energy neutrons spreads in time as it is cooling down. This process is highly non-linear and, therefore, influences the pulse shape (see Fig. 3.2). In the beginning the neutrons loose a high percentage of their respective energies, while toward the end collisions get less and less efficient. A moderator is termed fully *coupled* if neutrons of practically any energy can pass freely between the reflector surrounding the target and the moderator. If the shape of the moderator is optimized, then this procedure allows thermalizing all neutrons that are hitting the moderator. Depending on wavelength full moderation leads to pulses between 100 and 350 μs. If shorter pulses are required, then the moderator has to be *decoupled* from the reflector. This is done by surrounding the moderator on all sides that are exposed to the reflector by a shield of absorbing material. All neutrons below a certain threshold velocity, which is determined by the absorption edge of the absorber, are denied entrance to the moderator. This decoupling cuts off the tail of intensity that would otherwise arise from those late arriving neutrons which were already pre-moderated in the reflector. The moderation volume can be further reduced by placing an absorbing plate directly inside the moderator (see Fig. 3.2). The volume opposite to the beam ports can then no longer contribute to the final stages of the moderation process. Reduced moderation volume translates into shorter residence times for the neutrons and thus shorter pulses. It is obvious that this so-called *moderator poisoning* has a high price in intensity. Due to this unavoidable trade-off of pulse length and intensity, the design

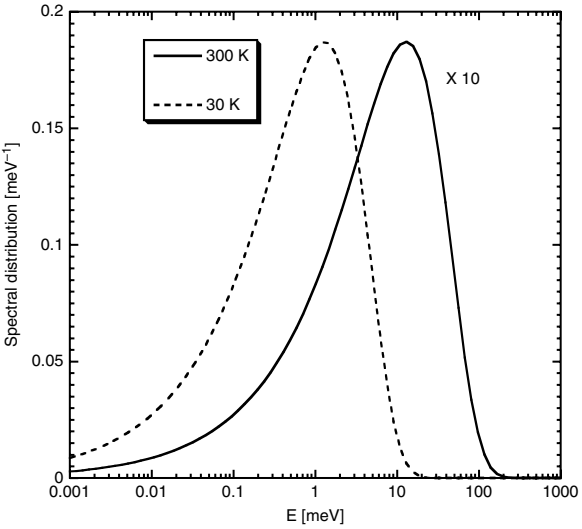

Fig. 3.3 Maxwell–Boltzmann energy distribution for moderator temperatures of 300 and 30 K, respectively. The y-axis has to be scaled by the integrated flux Φ_{thermal}. For better comparison, the 300 K curve has been multiplied by a factor 10

of the moderator around the target is of paramount importance for the performance of a pulsed source.

The colder the moderator, the lower the mean energy of the neutrons and the narrower the energy distribution (see Fig. 3.3). A colder spectrum thus has a higher flux for a given energy interval ΔE in the region of the spectrum's maximum.

As moderated neutrons are in thermal equilibrium with a bath at temperature T, their mean energy as given by Eq. (3.3) will automatically match the mean kinetic energy of any material at that temperature. In quantum mechanical terms, the neutron energy is comparable to the energy of excitations getting thermally populated at that temperature. This is a very important fact for neutron spectroscopy. It means that the energy exchange with the sample during scattering is often[7] of the same order of magnitude as the neutron energy itself. The relative energy resolution $\Delta E/E$ can thus be rather relaxed. The above argument holds for any fully moderated particle. The peculiarity of the neutron resides in the fact that it has a concomitant wavelength (from about 0.5 to 20 Å) which probes equally the right length scales, that is, inter-atomic distances and crystal lattice spacings. This is due to the mass of the neutron. A generally accepted classification scheme for neutron energies is given as follows: *epithermal* above 500 meV, *hot* from 100 to 500 meV, *thermal* from 10 to 100 meV, and *cold* below 10 meV. Apart from the moderated spectrum described

[7] There are naturally exceptions to this. Low-energy excitations are populated at temperatures very much lower than the lowest moderation temperature. Their investigation requires a high relative energy resolution $\Delta E/E$ using, for example, a backscattering spectrometer (see Section 3.4.2).

by Eq. (3.6), beams contain varying amounts of fast and epithermal neutrons that escape the moderator before they become fully thermalized. As these neutrons contribute to the background, special care is taken to eliminate them before the beam arrives at the instrument.

3.3 Neutron Beams

Once the neutrons are produced and moderated to appropriate temperatures, they have to be transported with the right characteristics to the sample. Before going into the description of the technical possibilities for beam transport and beam shaping, we would like to introduce a statistical description of the beams. This will allow us to give precise meaning to the concepts of nominal beam parameters, monochromaticity and divergence. The correct mathematical description of the beam is equally important for correctly relating the measured intensities to their theoretical interpretation in terms of the scattering function. A description of the beam with the help of distribution functions has the additional merit that it follows the logic of modern simulation packages. This description is based on the incoherent nature of the neutron beam (see above) and thus cannot describe interference phenomena, as observed when splitting a beam into coherent parts with the help of perfect crystals [11].

3.3.1 Statistical Description

The neutrons extracted from the moderator through a beam port can be considered an expanding gas. As the neutrons do no longer interact with the bath, they are out of thermal equilibrium. For such a beam of neutrons to be fully defined requires that we know at any point in space and time the probability $p(\vec{k};(\vec{r},t))$ of detecting a neutron with direction $\hat{k} = \vec{k}/|\vec{k}|$ and energy $E(k)$; that is, we know the phase space density $\mathrm{d}N$ of the beam at any point along its trajectory. In steady - state operation, there is no explicit time dependence and thus the parameter t can be ignored. This is not at all the case for pulsed beams.

The probability distribution has to be normalized such that the integral

$$N(t) = \int_K \int_R p(\vec{k};(\vec{r},t))\mathrm{d}^3k\mathrm{d}^3r \tag{3.8}$$

gives the number of neutrons detectable at a given time in the real space element $R = \Delta x\Delta y\Delta z$, possessing wave-vectors falling into the k-space element $K = \Delta k_x\Delta k_y\Delta k_z$. Therefore, $p(\vec{k};(\vec{r},t))$ incorporates the neutron production (see Eq. 3.2) and all beam shaping that has occurred upstream from $\vec{r}$.

The *particle current* of a beam passing through an area S is determined by its density and velocity distribution. It is given in the most general case by the surface

integral

$$I(t) = \int \left[\int_S p(\vec{k}; (\vec{r,} t))(\vec{v_k} \cdot \mathrm{d}\vec{a}) \right] \mathrm{d}^3k = \frac{\hbar}{m} \int \left[\int_S p(\vec{k}; (\vec{r,} t))(\vec{k} \cdot \mathrm{d}\vec{a}) \right] \mathrm{d}^3k, \quad (3.9)$$

where $\mathrm{d}\vec{a}$ is the infinitesimal surface vector, which is locally perpendicular to S.

In the case of a rectangular area A perpendicular to $\hat{z}$, Eq. (3.9) reduces to

$$I(t) = \frac{\hbar}{m} \int_A \mathrm{d}x \mathrm{d}y \int p(\vec{k}; (x, y, t)) k_z \mathrm{d}^3k, \quad (3.10)$$

which in case of a homogeneous distribution of wave-vectors over the beam cross section A further simplifies to

$$I(t) = A \frac{\hbar}{m} \int p(\vec{k}; t) k_z \mathrm{d}^3k = A \cdot n \cdot \bar{v}_z. \quad (3.11)$$

In the last equation we have introduced the mean velocity of the beam along $\hat{z}$ and the particle density n. If we divide the current by the area A, we get the *flux* $\Phi(t)$ of the beam

$$\Phi(t) = \frac{\hbar}{m} \int p(\vec{k}; t) k_z \mathrm{d}^3k = n \cdot \bar{v}_z, \quad (3.12)$$

that is, the number of particles passing along $\hat{z}$ per unit area and second. A beam is the better defined the narrower the distribution function. A *monochromatic beam* contains, for example, only neutrons within a well-defined energy or wavelength band. In general, the monochromaticity is not perfect, and the energies are distributed around a nominal energy[8] defined as

$$E_0(\vec{r,} t) = \frac{1}{N} \int_K \int_R p(\vec{k}; (\vec{r,} t)) \frac{\hbar^2 k^2}{2m} \mathrm{d}^3k \mathrm{d}^3r, \quad (3.13)$$

with the standard deviation

$$\Delta E(\vec{r,} t) = \sqrt{\frac{1}{N} \int_K \int_R p(\vec{k}; (\vec{r,} t)) \left(\frac{\hbar^2 k^2}{2m} - E_0 \right)^2 \mathrm{d}^3k \mathrm{d}^3r}. \quad (3.14)$$

ΔE is the absolute and

$$\frac{\Delta E}{E_0} = 2 \frac{\Delta \lambda}{\lambda}, \quad (3.15)$$

[8] Throughout this chapter we will denote the nominal values by the subscript zero and the standard deviations or full widths half maximum (FWHM) by the prefix Δ.

the relative energy spread of the beam. Both evolve in general along the beam as a function of position and time. In the same way we have defined the mean energy, it is possible, to define the nominal wave-vector direction $\hat{k}_0(\vec{r}, t)$ of the beam. The angular deviations $(\Delta\hat{k}_x(\vec{r}, t), \Delta\hat{k}_y(\vec{r}, t), \Delta\hat{k}_z(\vec{r}, t))$ from the mean direction of the beam are called the *divergence* of the beam.

3.3.2 Scattering of the Beam

The task of neutron scattering consists of measuring the changes in the probability distribution $p(\vec{k})$ due to the interaction with a sample. In simple terms, we want to determine the angular deviation of a neutron beam concomitantly with its change in energy and spin. As neutrons cannot be labeled,[9] this requires the knowledge of the direction, energy, and spin of the neutron beam both before and after the scattering event.

$$\frac{\mathrm{d}^2\sigma}{\mathrm{d}\Omega \mathrm{d}E_f} = \frac{k_f}{k_i} S(\vec{Q}, \hbar\omega), \tag{3.16}$$

that is, the fraction of neutrons scattered per second into a solid angle element $\mathrm{d}\Omega$ with energies comprised between E_f and $E_f + \mathrm{d}E_f$.[10] The scattering cross section has thus the dimension of an area. In Eq. (3.16) we have related the double differential scattering cross section to the *scattering function* $S(\vec{Q}, \hbar\omega)$ with

$$\vec{Q} = \vec{k}_i - \vec{k}_f, \tag{3.17}$$

$$Q^2 = k_i^2 + k_f^2 - 2k_i k_f \cos 2\theta, \tag{3.18}$$

and

$$\hbar\omega = E_i - E_f = \frac{\hbar^2}{2m}\left(k_i^2 - k_f^2\right). \tag{3.19}$$

The triple of vectors $(\vec{Q}, \vec{k}_i, \vec{k}_f)$ forms a triangle in the scattering plane, which is called the *scattering triangle* (see Fig. 3.5). The intensity in the detector per final energy interval can be written as [12]

[9] If the interaction with the sample produces a deterministic change in one of the variables, e.g., if it does not change the spin state of the neutron, then we can use this variable as a label to encode one of the others, e.g., the energy. This principle is at the origin of the spin - echo technique (see Section 3.4.8).

[10] This is equal to the number of neutrons scattered per second into a solid angle element $\mathrm{d}\Omega$ with energies comprised between E_f and $E_f + \mathrm{d}E_f$ and normalized to the incoming flux.

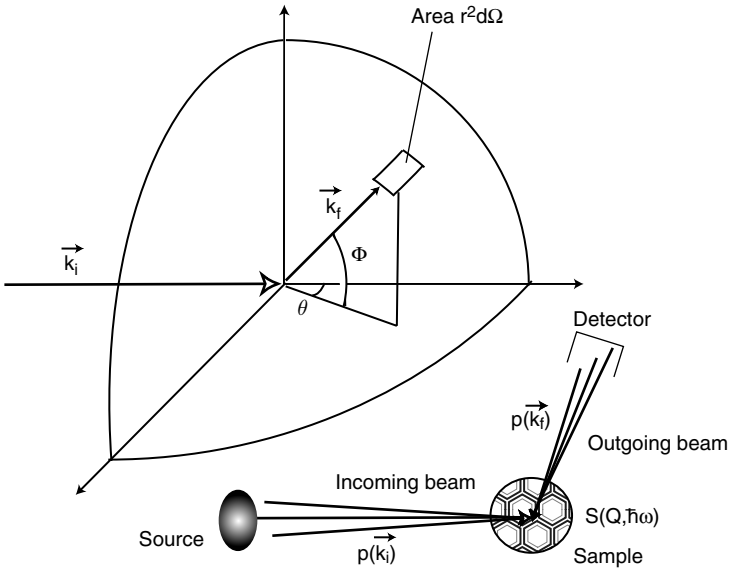

Fig. 3.4 Scattering of a beam by the sample. In the classical approach, the scattering is described by the double differential cross section giving the probability that a normalized flux of neutrons of incident wave-vector $\vec{k}_i$ is scattered into a solid angle element $\mathrm{d}\Omega$ perpendicular to the direction $\hat{k}_f$ with energies comprised between $E_f = \hbar^2 k_f^2/2m$ and $E_f + \mathrm{d}E_f$, that is, between $(\hbar^2/2m)k_f^2$ and $(\hbar^2/2m)(k_f^2 + 2k_f\ \mathrm{d}k_f)$. If we choose the coordinate system such that $\hat{k}_f = \hat{k}_z^f$, then $\mathrm{d}\Omega = \mathrm{d}k_x^f\ \mathrm{d}k_y^f/k_f^2$. In practice the incoming beam of neutrons has a distribution $p(\vec{k}_i;t)$ in energy and direction, depending on how the neutrons were moderated and then shaped by the beam transport. In the same way the neutrons detected will have a distribution $p(\vec{k}_f;t)$ arising from the beam shaping during the transport from the sample to the detector and from the detector efficiency. The beam characteristics described by $p(\vec{k}_i;t)$ and $p(\vec{k}_f;t)$ are responsible for both the statistics and the resolution of the measurements

$$I(E_f)\mathrm{d}E_f \propto \int\int p(\vec{k}_i)S(\vec{Q},\hbar\omega)p(\vec{k}_f)\mathrm{d}^3k_i\mathrm{d}^3k_f. \tag{3.20}$$

For simplicity the distributions $p(\vec{k}_i)$ and $p(\vec{k}_f)$ have been assumed to be homogeneous over the sample volume and not to depend on time, making the space integration trivial.

Equation. (3.20) has a simple interpretation if we think in terms of transport of neutrons to and from the sample. The distribution $p(\vec{k}_i)$ describes the probability of neutrons with wave-vector $\vec{k}_i$ to arrive at the sample after having been produced at the source and shaped by the various optical elements (guides, choppers, monochromators). It includes thus, for example, the source brilliance. The distribution $p(\vec{k}_f)$ describes the probability of neutrons leaving the sample being detected in the detector element corresponding to the solid angle $\mathrm{d}\Omega$ and energy interval between E_f and $E_f + \mathrm{d}E_f$. Possible obstacles are filtering devices like slits and analyzers or

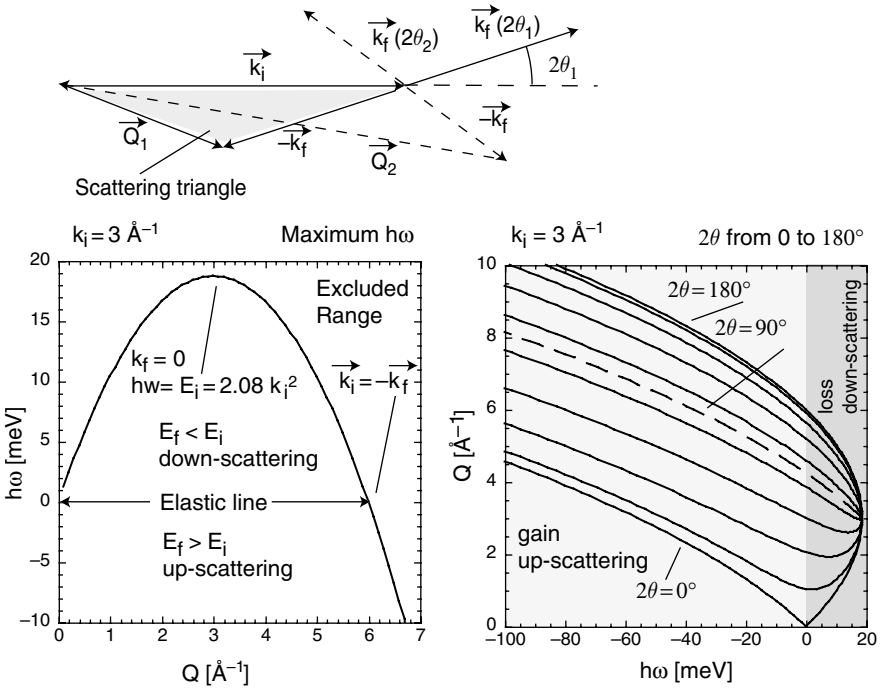

Fig. 3.5 Dynamic range of a scattering experiment. The wave-vector transfer $\vec{Q}$ is given by the vector addition $\vec{k}_i - \vec{k}_f$, while the energy transfer is determined by $\hbar\omega = E_i - E_f$. Both quantities are not independent. For a given k_i there are always combinations $(\vec{Q}, \hbar\omega)$ for which the scattering triangle does not close, that is, for which the *kinematic conditions* are not fulfilled. The example presented here shows on the left - hand side the maximum energy transfer that can be obtained as a function of $Q = |\vec{Q}|$ with a k_i of 3 Å^{-1}. On the right - hand side, we plot the energy transfer associated with a given Q under specific scattering angles 2θ (angles increase from 0° to 180° in 20° steps). These are the $(Q, \hbar\omega)$ trajectories that one would measure with a direct geometry time-of-flight spectrometer (see Section 3.4.3). Everything outside the 0 and 180° lines is inaccessible to the experiment. These lines, thus, limit the field of view of the measurement in reciprocal space

inefficient detectors. $S(\vec{Q}, \hbar\omega)$ describes the transmutation of the beam via the sample. It gives the flux normalized probability of an incident neutron with wave-vector $\vec{k}_i$ being scattered into an outgoing neutron with wave-vector $\vec{k}_f$. $S(\vec{Q}, \hbar\omega)$ is completely independent from how we set up our spectrometer. It is a function entirely determined by the sample and is in this sense more fundamental than the scattering cross section.[11] The determination of $S(\vec{Q}, \hbar\omega)$ is the goal of any experiment. The description of its properties is the main task of the theory of neutron scattering as, e.g., described by Squires [13], Lovesey [14], or Price and Sköld [15].

[11] The scattering function as defined here does still contain the interaction potential of the neutron with matter. In other words, it contains the scattering length b_l of the nuclei and has, therefore, the unit of area per energy.

Equation (3.20) can be cast in the form [16].

$$I(E_f)\mathrm{d}E_f \propto \int\int R(\vec{Q}-\vec{Q}_0, \hbar\omega - \hbar\omega_0) S(\vec{Q}, \hbar\omega)\mathrm{d}^3Q\mathrm{d}\hbar\omega. \tag{3.21}$$

with

$$R(\vec{Q}, \hbar\omega) = \int\int p(\vec{k}_i)p(\vec{k}_f)\delta\left(\vec{Q}-(\vec{k}_i-\vec{k}_f)\right)\delta\left(\hbar\omega - \frac{\hbar^2}{2m}(k_i^2-k_f^2)\right)\mathrm{d}^3k_i\mathrm{d}^3k_f. \tag{3.22}$$

The *resolution function* $R(\vec{Q}, \hbar\omega)$ gives the probability of finding combinations of neutrons $\vec{k}_i$ and $\vec{k}_f$ in the beam, such that $\vec{k}_i - \vec{k}_f = \vec{Q}$ and $E_i - E_f = \hbar\omega$. The variables $\vec{Q}_0$ and $\hbar\omega_0$ denote the most probable $\vec{Q}$ and $\hbar\omega$ values. They are the centers of gravity of the resolution function about which the measurement is conducted. In order to retrieve the physically relevant quantity $S(\vec{Q}_0, \hbar\omega_0)$, the measurement has to be de-convoluted with the resolution function. In particular, changes in the overall number of neutrons present in the incoming and detected beams and described mathematically by the resolution volumes

$$V_i = \int p(\vec{k}_i)\mathrm{d}^3k_i \qquad \text{and} \qquad V_f = \int p(\vec{k}_f)\mathrm{d}^3k_f \tag{3.23}$$

have to be corrected for.

The scattering of a neutron by matter can to the first order be described as the superposition of spherical waves

$$\psi_{\text{out}}(\vec{r}) \propto \sum_l \frac{b_l}{|\vec{r}-\vec{r}_l|}\mathrm{e}^{ik|\vec{r}-\vec{r}_l|}\psi_{\text{in}}(\vec{r}_l) \tag{3.24}$$

$$\propto \int p(\vec{k}_i)\sum_l \frac{b_l}{|\vec{r}-\vec{r}_l|}\mathrm{e}^{ik|\vec{r}-\vec{r}_l|}e^{i\vec{k}_i\vec{r}_l}\mathrm{d}^3k_i, \tag{3.25}$$

with $\vec{r}_l$ denoting the position of the scatterer l and b_l the scattering length. For simplicity, we assumed static scatterers leading to elastic scattering $k = k_f = k_i$. The source of the scattered spherical waves is the incoming neutron wave ψ_{in}, which in our description of the beam is given as a distribution in $\vec{k}_i$. Thus atoms along the wavefront, that is, atoms finding themselves at positions of constant $\vec{k}_i \cdot \vec{r}_l$, scatter in phase.[12] Due to the distribution in direction and wavelength of $\vec{k}_i$ (and $\vec{k}_f$) the interference of the scattered waves is smeared out if the distance between

[12] If we observe the scattered wave ψ_{out} at the detector, we must include in Eq. (3.25) the description of the scattered beam as a function of $\vec{k}_f$. This includes as outlined above the probability of a neutron $\vec{k}_f$ reaching the detector and leads us to an expression equivalent to Eq. (3.21).

the scatterers becomes too large. In this picture, the resolution function describes the extension in space and time of the so-called *coherence volume*. Scattering from atoms placed within the coherence volume has to be added coherently, that is, by respecting the phase [17]. Scattering originating from atoms belonging to different coherence volumes can be simply added as intensity. This implies that we have no access to correlations from a given atom to the atoms found outside the coherence volume. The coherence volume is thus the instrument's *field of view* in direct space.

We will see in the following sections that the resolution $\Delta Q_i, i = x, y, z$ and $\hbar\Delta\omega$ and thus the associated coherence volumes increase strongly with longer wavelengths. This is not surprising as the beam definition is always done relative to the nominal neutrons; that is, relative resolutions like $\Delta Q/Q$ and $\Delta\omega/\omega$ are similar over a large range of instrument variables. Longer wavelengths, however, imply a reduced range of accessible $(\vec{Q}, \hbar\omega)$ points. For example, in the case of elastic scattering, $|\vec{k}_i| = |\vec{k}_f|$, the maximum Q-transfer that can be obtained is $2\vec{k}_i$ for $\vec{k}_f = -\vec{k}_i$. Equally neutrons cannot lose more than their total energy so $\hbar\omega < E_i$. By deducing $|\vec{k}_i|$, we reduce the *dynamic range* of the scattering experiment; that is, we reduce the *field of view* of our experiment in reciprocal space (see Fig. 3.5). Large fields of view in direct and reciprocal space are thus conflicting requirements.

3.3.3 Beam Shaping

As $S(\vec{Q}, \hbar\omega)$ is the relevant quantity to be extracted from the data, it is obvious from Eq. (3.20) that the better defined the beam, that is, the narrower the distributions $p(\vec{k}_i)$ and $p(\vec{k}_f)$, the more accurate the measurement, that is, the higher the resolution and the larger the coherence volume. This requires intense beams of highly collimated (sharp distribution in $\vec{k}/|\vec{k}|$) and highly monochromatic beams (sharp distribution in E).[13] The whole art of neutron scattering instrumentation consists of optimizing the neutron beams for the scientific task at hand. Ideally, we want an instrument that offers high luminosity at high resolution over a broad range of energies and momentum transfers, that is, with a large dynamical range.

---

[13] One may ask why we do not use energy - sensitive detection. This would avoid tailoring the outgoing beam and thus increase the overall luminosity of the experimental set-up. Energy - sensitive detection requires a correlation between the detector output signal and the neutron energy. A typical energy - sensitive detector is a gas chamber for charged particles. The principle works because the energies of the particles are orders of magnitude larger than the ionization energies required to leave a trace of their trajectory in the gas. For a similar technique to work with thermal neutrons, we would require a system that possesses trackable excitations restricted to the sub-meV range as any meV excitation would completely ruin the energy sensitivity. Such systems are difficult to conceive. An alternative to tracking the trajectory via local inelastic excitation of a medium is a system based on elastic scattering. Incoming neutrons are scattered into different angular regions depending on their energies. The correlation between angle and energy is based on the Bragg-law (see Section 3.3.5) and the scattering can be produced by oriented powders surrounded by position - sensitive detectors. Some pioneering work is currently carried out in this area. The problem with such devices lies with the fact that they are quite cumbersome and difficult to realize for large-area detectors.

The economic way of doing this would consist of producing only those free neutrons that suit the purpose, that is, those that have the right energy and the right direction. This is, however, not possible with current neutron sources, which, as we have seen, produce a gas of free neutrons with little to no directionality and a rather broad distribution in energy. Despite this fact, instrument design cannot be dissociated from the neutron source. In particular, the moderation process of the neutrons and their time structure in the case of pulsed sources are of prime importance for the performance of an instrument suite [18].

Dealing with a neutral particle, the only experimental possibility of manipulating a neutron in vacuum is by acting onto its magnetic moment via strong magnetic fields. This technically demanding method of creating strong continuous or alternating magnetic fields is presently only employed for polarized neutron instruments. In the case of normal, that is, unpolarized beams, the neutron is manipulated via the absorption or nuclear and/or magnetic scattering it experiences in matter. Absorption is a brute force method that allows a beam to be tailored in time and space by simply eliminating undesirable neutrons through screens. A more efficient shaping of the beam can be achieved by exploiting the specular reflection of neutrons at an interface or the Bragg reflection of neutrons from crystal lattices. In particular, this allows spacial or angular beam compression (one always at the expense of the other, as the phase space density is a conserved quantity) and energetic filtering. If the beam is pulsed, efficient way of filtering neutrons is provided by discriminating them according to their velocities by measuring the difference in time of flight.[14]

3.3.4 Mirrors and Guides

Specular reflection of neutrons has been observed as early as 1944 by Fermi and Zinn [19] and can be described via the *index of refraction n* of the neutrons.[15] The index of refraction of a medium is defined as the ratio of the k-vector modulus in the medium with respect to its value k_0 in vacuum and reflects the fact that the speed of the particle and thus its kinetic energy has to adapt to a variation in the potential energy as a consequence of overall energy conservation. For a neutron, the interaction of the neutron with the nuclei can be described by the *Fermi pseudo-potential*

$$V(\vec{r}) = \frac{2\pi\hbar^2}{m} \sum_l b_l \delta(\vec{r} - \vec{R}_l), \qquad l = 1, \ldots, N, \tag{3.26}$$

with $\vec{R}_l$ denoting the site of the nuclei l. If the medium can be considered homogeneous, then the *scattering density function* reduces to

[14] A more detailed discussion of the different filters can, for example, be found in [20].
[15] For a historical account of the early experiments with neutrons, see [21].

$$\sum_l b_l \delta(\vec{r} - \vec{R}_l) = \sum_i N_i b_i, \tag{3.27}$$

with N_i denoting the number density of scatterers of type i. The *index of refraction* n can be directly related to the density of scattering amplitude $\sum_i N_i b_i$ via

$$n = \frac{k}{k_0} = \sqrt{1 - \frac{4\pi}{k_0^2} \sum_i N_i b_i} = \sqrt{1 - \frac{\lambda^2}{\pi} \sum_i N_i b_i}. \tag{3.28}$$

The quantity $\sum_i N_i b_i$ is equally called the *scattering length density* (SLD) of the material. Values of b are typically in the range of 10^{-15} m and $N \approx 10^{29}$ per m^3. For $\lambda = 1$ Å we can estimate the order of magnitude of the expression $\lambda^2 \sum_i N_i b_i$ as $\approx 10^{-6}$. Using $\sqrt{1-x} \approx 1 - \frac{1}{2}x$ for small x leads to

$$n = \frac{k}{k_0} = 1 - \frac{\lambda^2}{2\pi} \sum_i N_i b_i. \tag{3.29}$$

The index of refraction of thermal and even cold neutrons is, therefore, extremely close to one if compared to that of ordinary light. This reflects the weak interaction of neutrons with matter. As in the case of light, we get total reflection if

$$\cos\theta_c = n. \tag{3.30}$$

As $|n - 1|$ is small for neutrons we may write

$$n^2 \approx 1 - \frac{\lambda^2}{\pi} \sum_i N_i b_i \tag{3.31}$$

to obtain

$$1 - (\sin\theta_c)^2 = 1 - \frac{\lambda^2}{2\pi} \sum_i N_i b_i, \tag{3.32}$$

and thus

$$\sin\theta_c = \sqrt{\frac{\sum_i N_i b_i}{\pi}} \lambda. \tag{3.33}$$

θ_c is called the *critical angle* of the material. Total external reflection (contrary to light $n < 1$) inside a channel is used to transport neutrons over large distances.

Nickel, due to its large coherent scattering cross section and thus rather large critical angle of $\theta_c = 0.1^\circ/\text{Å}$, is a material of choice for these *neutron guide* applications. The transport is the more efficient the longer the wavelength, since as due to the increased critical angle at longer wavelength larger divergences can be tolerated. The critical angle can be greatly enhanced by using multi-layered materials, such as those made up of Ni and Ti. Using modern technology, these so-called *supermirrors* have elevated reflectivity of above 80% up to angles several times larger than that of natural Ni. Supermirror guides are usually classified according to their m value, with m defined via the relation $\theta_c = m \cdot \theta_c^{\text{Ni}}$. An $m = 2$ guide thus transports a divergence twice as high as natural Ni.[16]

Specular reflection does not only allow transporting neutrons, but also is an equally good means of *focusing* beams in space at the expense of angular divergence. This is achieved by bending the mirrors. The form of the neutron channel is decisive for its performance. Due to material imperfections, reflection is never 100% even below the critical angle. The number of reflections in the guide is to be minimized. This can, e.g., be achieved by using the so-called *ballistic guides* [8, 22] (see Fig. 3.6). These guides open up considerably in cross section over the main part of the length, reducing the divergence of the beam at the expense of spacial dilution. This reduces the number of reflections. Shortly before the sample the neutrons are refocussed.

An important task of neutron guides is to reduce the amount of unwanted fast neutrons at the instrument. They are, therefore, often curved in such a way that there is no direct view of the moderator; that is, any neutron arriving at the instrument has been forced to reflect at least once.

It is not trivial to predict the transmission properties of a neutron guide exactly. The distribution $p(\vec{k})$ at the exit of the guide does not only depend on the reflectivity of the mirrors but also equally on its filling at the entrance. It, therefore, cannot be generally assumed that the divergence transported is only a function of the critical angle–as we will do for convenience in some of the following sections. $p(\vec{k})$ may not even be homogeneous over the guide cross section. This is necessarily the case for a curved guide where the curvature introduces a symmetry break between the inner and the outer side of the guide.

Any straight neutron guide can be considered a *collimator* as it limits the divergence of the beam at the outlet to the critical angle $\pm\theta_c$. This holds provided that every neutron with a larger divergence cannot pass the guide without reflection. This is the case if the ratio of the width a to the length l of the guide satisfies the relation $a/l \leq \tan\theta_c$. If the coating is not reflecting at all, that is, if the walls consist of neutron absorbing materials like Cd or Gd, then the collimation is achieved purely by geometric means and we speak of a Soller collimator. To avoid excessively long collimation distances to achieve a compact design, multichannel collimator

[16] The appropriate choice of the multi-layer material allows constructing a guide that in a magnetic field allows to reflect only one spin component of the material. It thus can be used as a polarizing device.

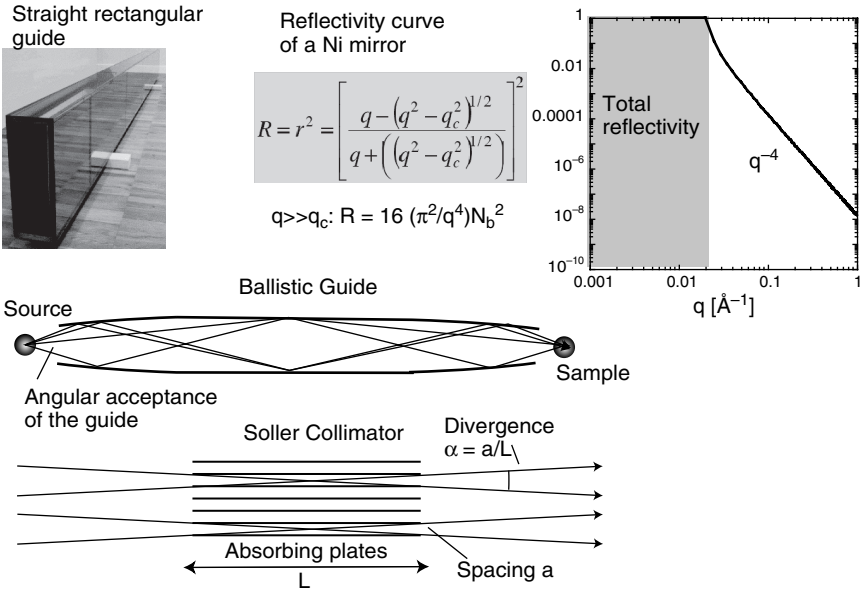

Fig. 3.6 Neutron guides. The reflection occurs on coated glass substrates that are assembled to form closed channels. The reflectivity is one below the critical momentum transfer q_c and drops off rapidly with larger q (that is, with larger reflection angles). Natural Ni is the reference coating material. Supermirror guides are guides featuring a multi-layer coating that pushes the critical angle to higher values. Every reflection is in practice connected with losses. The geometry of the guide is, therefore, of prime importance for its performance. Ballistic guides are very efficient transport media over large distances [8, 22]. They feature an anti-trumpet section at the beginning of the guide to reduce the beam divergence. This leads to fewer reflections that in addition take place at small angles in the long straight section. A trumpet before the sample focuses the beam to the original cross section, increasing the divergence to its original value

constructions are used, which allow a small a/l ratio to be kept over large beam cross sections. The individual channels are delimitated by neutron absorbers coated onto thin spacers. The disadvantage of a Soller collimator with respect to a guide is the fact that the transmission of a neutron depends on the point of entry into the collimator giving a triangular transmission[17] as a function of divergence angle θ. This reduces the overall transmitted flux in comparison to a guide that ideally has a transmission equal to one for $|\theta| \leq \theta_c$.

3.3.5 Crystal Monochromators

Neutrons are particle waves and as such are diffracted by gratings. If the grating is composed by the lattice planes of a crystal, then the diffraction can be described as

[17] In practice, it turns out that due to imperfections the transmission can be well described by a Gaussian distribution.

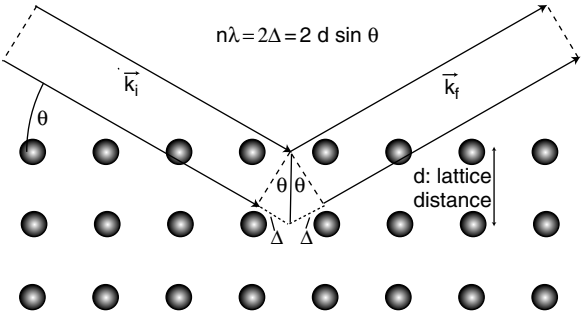

Fig. 3.7 Bragg scattering. In the case of a continuous beam, energy selection is achieved by exploiting the fixed relation between the wavelength of neutrons reflected from the crystal planes and the direction of reflection. The reflection is said to be wavelength dispersive. Under a given Bragg angle θ, a particular wavelength $\lambda(\theta)$ is observed. The d-spacing has to be chosen with care, as it determines for a given wavelength the Bragg angle and thus, according to Eq. (3.37), the resolution of the filter.

a reflection governed by the *Bragg equation*

$$n\lambda = 2 \cdot d \cdot \sin\theta, \tag{3.34}$$

with the *scattering angle* 2θ denoting the angle spanned by the incoming $\vec{k}_i$ and scattered $\vec{k}_f$ neutron wave vectors. d is the distance between the lattice planes and n denotes the order of the Bragg reflection. The Bragg equation states the familiar fact that positive interference from planes of scattering is obtained when the optical path difference is a multiple n of the wavelength (see Fig. 3.7). The crystal placed at a given angle with respect to the beam thus acts as an energy or wavelength filter. The Bragg reflection of neutrons by a single crystal has been observed as early as 1936 [23] and used by Zinn in 1946 as a monochromator [24].

As we will see in the sections on instrumentation, it is very helpful to reformulate the Bragg equation in reciprocal space

$$\vec{\tau} = \vec{k}_f - \vec{k}_i, \qquad |\vec{k}_i| = |\vec{k}_f|, \tag{3.35}$$

with $\vec{\tau}_{hkl} = h\vec{a}_1^* + k\vec{a}_2^* + l\vec{a}_3^*$ denoting the lattice vector in reciprocal space, that is, the vector that is perpendicular to the planes and has a length $|\vec{\tau}_{hkl}| = 2\pi/d_{hkl}$. In other words, Bragg scattering occurs when $\vec{k}_i$, $\vec{k}_f$, and τ form an isosceles triangle with τ as the base (see Fig. 3.8). The manifold of $\vec{k}$-vectors that can be reflected is a two-dimensional surface in $\vec{k}$-space defined by the requirement that the projection of $\vec{k}$ onto $\vec{\tau}$ equals the constant $\tau/2$.

The band that is cut out from the incoming spectrum has a width defined by the beam divergences $\Delta\theta$ and uncertainties in the lattice spacing Δd:

$$\Delta\lambda = 2 \cdot d \cdot \cos\theta\Delta\theta + 2 \cdot \sin\theta\Delta d = (\lambda\cot\theta)\Delta\theta + \frac{\lambda}{d}\Delta d. \tag{3.36}$$

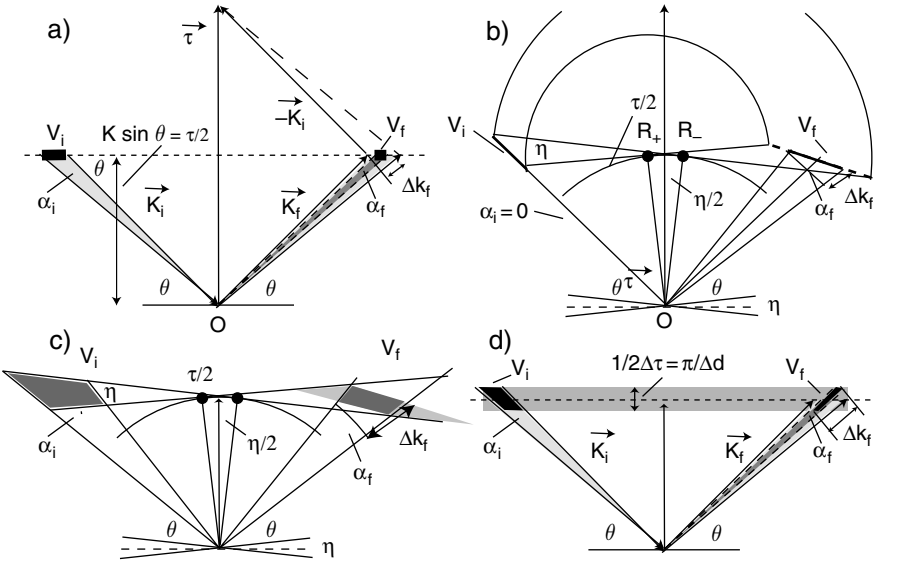

Fig. 3.8 Description of Bragg scattering in reciprocal space. The Bragg equation is satisfied, if both the incoming and the reflected beam have a projection of $k \sin\theta = \tau/2$ onto the lattice vector $\vec{\tau}$. This gives a one-to-one match of $\vec{k}_i$ onto $\vec{k}_f$. The incoming beam has necessarily a finite divergence α_i leading to a divergent reflected beam. This is indicated by the *lightly shaded areas* in figure (**a**). The finite divergence entails a spread in the length of the outgoing wavevectors Δk_f, that is, a finite width in energy of the produced beam. This width can be reduced by decreasing the divergence of the outgoing beam with the help of a collimator (*dark shaded area*). The incoming phase space element V_i will translate into a phase space element V_f after the reflection, defined by the interesction of the dark shaded area with the $\tau/2$-line. It becomes immediately evident that for given divergences the monochromaticity is increasing with the Bragg angle θ and thus depends strongly on the lattice spacing d. If the crystal is not perfect, then there will be a distribution of the orientation of the lattice planes called mosaic described by η. Graphically, this corresponds to tilting the diagram of figure (**a**) by $\pm\eta/2$ around the origin O. As shown in figure (**b**) the image of a tightly collimated incoming phase space element V_i can be constructed by mirroring the shortest and longest $\vec{k}_i$ with respect to the lines $O - R_-$ and $O - R_+$, respectively. It is important to note that the obtained phase space element V_f is inclined with respect to $\vec{k}_f$. In figure (**c**) we show the general situation of an incoming beam of divergence α_i being reflected by a mosaic crystal into an outgoing beam of divergence α_f. The area of V_f reflects the intensity of the outgoing beam, provided the phase space element V_i is fully filled. The experimental set-up is optimized if V_f is maximum for a required $p(\vec{k}_f)$, that is, for a required $\vec{k}_f$ and Δk_f. Figure (**d**) shows the situation in phase space for a crystal with varying d-spacing. This can be achieved via a gradient in the chemical composition of the crystal or by straining the crystal mechanically or thermally. The volume of V_f is given by the cross section of the *shaded area* arising from the divergence with the one arising from the distribution in τ

The width $\Delta\lambda$ or in terms of relative resolution,

$$\frac{\Delta\lambda}{\lambda} = \cot\theta\Delta\theta + \frac{\Delta d}{d}, \tag{3.37}$$

gives the width of the distribution function $p(k)$ defining the beam after the crystal monochromator in terms of the length of the $\vec{k}$-vector.[18] For a beam divergence of 1° and scattering under $2\theta = 90^\circ$, we get a wavelength resolution of about 1% from a perfect crystal. The resolution can be improved by better defining the angular distribution of the beam. This is done with the help of collimators, that is, arrays of absorbing neutron channels (see above), which allow defining independently the divergence $\Delta\vec{k}_i$ and $\Delta\vec{k}_f$ of the incoming and scattered beam. This naturally comes at the cost of a strongly reduced beam intensity (see Fig. 3.8). For a given divergence, $\Delta\theta$. The best resolution, that is, the narrowest wavelength band, is obtained at $2\theta = 180^\circ$, that is, in backscattering geometry. We will discuss this in more detail in Section 3.4.2.

As the Bragg scattering is dispersive, it introduces a strong correlation between wavelength and angle into the beam. In reciprocal space, this means that the phase space volume is *inclined* with respect to the outgoing wave-vector $\vec{k}_f$. In practical terms, this break in rotational symmetry about the beam direction implies that left and right are no longer equivalent. This has important consequences for setting up the instruments.

For most practical applications the angular acceptance of an ideal crystal is too small to make efficient use of a divergent large-size beam. To overcome the problem, the crystals are processed in order to introduce either a variation in the lattice spacing d or a distribution of crystal orientations created by defects in the single crystal. In reciprocal space (see Fig. 3.8), this implies introducing a spread either in the length or direction of $\vec{\tau}$. The Bragg equation (Eq. (3.35)) is, therefore, satisfied for rings of finite thickness in $\vec{k}$-space. Crystals composed of crystallites are called *mosaic crystals*. The angular distribution of crystallites can be determined experimentally by turning (rocking) the crystal through the Bragg angle in a monochromatic beam with sufficiently high angular resolution. The probability of finding a crystallite with an orientation $\theta + \Delta\theta$ is given by the thus measured intensity as a function of angle (rocking curve). It normally is well described by a Gaussian function

$$W(\Delta\theta) = \frac{1}{\eta\sqrt{2\pi}} \mathrm{e}^{-\frac{\Delta\theta^2}{2\eta^2}}. \tag{3.38}$$

η is called the *mosaicity* of the crystal and for most monochromators varies between 10 and 40 min of arc. Mosaicity is responsible for the fact that the distribution in wavelength after reflection from the crystal has a Gaussian form. This is very

[18] The shape of $p(\lambda)$ will naturally reflect the shape of the distributions $p(\theta)$ and $p(d)$. For simplicity we may assume both to be described by Gaussian functions.

important for the resolution of spectrometers based on filtering wavelength with crystals (see Section 3.4.1). The mosaicity does not, however, necessarily have to be isotropic. In many cases it is even desired to be low in the vertical direction where it would only lead to beam loss.

The above formulae apply to flat crystals. Modern crystal monochromators are large in size and composed of a large number of single plates that are oriented such as to direct the beam onto small sample areas (see Fig. 3.9).[19] This is particularly important for thermal or hot neutrons, where converging neutron guides are inefficient as focusing devices due to the low critical angle even for super-mirrors. These *vertically* and *horizontally focusing* monochromators accept by definition a large divergence. Despite this fact, the energy resolution can be preserved provided the source size (eventually limited by slits) is comparable to the focus spot (sample size) and the right geometry is chosen (*monochromatic focusing*) for the distances from source to monochromator and from monochromator to sample [25].

It is not trivial to predict the intensity of a beam reflected from a crystal. The crystallographic quantity playing the role of a linear reflection coefficient is given by

$$I_{hkl} = \frac{\lambda^3}{N_c^2 \sin^2\theta} |F_{hkl}|^2, \tag{3.39}$$

where the symbols N_c and F_{hkl} are the number of unit cells per unit volume of the crystal and the structure factor for the reflecting plane (hkl), respectively. The structure factor measures the strength of the interference arising from the scattering by various lattice planes and is given by

$$F_{hkl} = \sum_i b_i \mathrm{e}^{i\vec{\tau}_{hkl}\cdot\vec{R}_i} = \sum_i b_i \mathrm{e}^{2\pi i(hx_i+ky_i+lz_i)} \quad , i = 1, \ldots, r, \tag{3.40}$$

with $\vec{R}_i = x_i\vec{a}_1 + y_i\vec{a}_2 + z\vec{a}_3$ giving the positions of the r atoms in the primitive cell of the crystal. For a crystal of thickness l, the scattered fraction of the neutron beam is in first approximation given by $I_{hkl} \cdot l$; that is, it increases linearly with the crystal thickness.

In reality, this is not the case due to the problem of *extinction*. In a perfect crystal already the first few thousand lattice planes exhaust the original incoming spectrum. Planes lying deeper in the crystal see a strongly modified incoming beam consisting of the original plus multiply reflected beams that overlay coherently. This coherent superposition is not taken into account by the simple *kinematic theory* used to obtain Eq. (3.39) and leads to *dynamic diffraction theory* [11, 28]. Increasing the depth

[19] A good overview of focusing Bragg optics is given in [26].

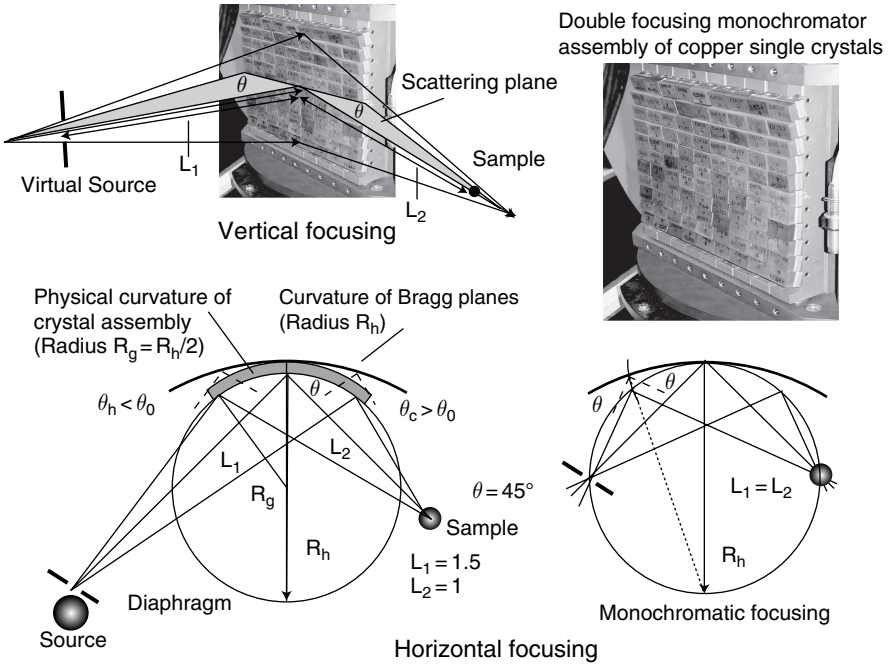

Fig. 3.9 Crystal monochromators. Large assemblies of crystals are used to focus the beam onto the sample. The example shown here is double focusing; that is, it compresses the beam both vertically and horizontally. The vertical curvature $\rho_v = 1/R_v$ satisfies the lens equation $2\sin\theta/R_v = 1/L_1 + 1/L_2$. The Bragg angle stays constant over the height of the monochromator. Vertical focusing is such always monochromatic. It produces an image of the vertical source of height $h_{\rm im} = h_{\rm s}(L_2/L_1)$, with a concomitant increase of the vertical divergence of the beam. The source height h_s is often virtual and is defined by diaphragms. For a guide the distance of the virtual source is defined by the divergence of the guide. For zero divergence, that is, for a fully parallel beam, $L_1 = \infty$. The size of the image is in practice always limited by the size of the crystallites used to build the monochromator. The horizontal focusing is more complex. The curvature $\rho_h = 1/R_h$ for the planes is determined via the relation $2/(R_h \sin\theta) = 1/L_1 + 1/L_2$. The Bragg angle generally varies over the monochromator. In the configuration shown, neutrons passing to the left of the center line have longer wavelengths; that is, they are hotter than the nominal ones ($\theta_h < \theta$), while to the right they are colder ($\theta_c > \theta$). Only in the case where $L_1 = L_2 = 1/R_h \sin\theta$ do we obtain a Bragg angle that is constant over the monochromator. This is called monochromatic focusing. The two focal points are said to lie on the *Rowland circle*. For every wavelength λ, there is exactly one possible set of positions for source and sample. As both the vertical curvature R_v and the horizontal curvature R_h depend on the Bragg angle θ, they have to be adjusted mechanically if the device is to be used for varying wavelengths. The phase space element impinging onto the sample can be further shaped by using a physical curvature of the crystal alignment with a radius different from the radius of the Bragg plane inclination. A particularly favorable case is $R_g = R_h/2$ [27]. Please note that for clarity of the graphical presentation, the dimensions of the monochromator are largely exaggerated. In practice, the distance from the monochromator to the sample is on the order of 1–2 m while the monochromators have typical dimensions of $20 \times 20\,{\rm cm}^2$. Exceptions are analyzers for backscattering instruments (see Section 3.4.2), which at distances of 1–2 m are up to 2 m high. In backscattering $\theta = 90^\circ$, and thus the situation becomes completely symmetric with respect to horizontal and vertical curvature ($L_1 = L_2 = L$ and $1/R_h = 1/R_v = 2/L$). In that case the Bragg angle is constant in all directions; that is, the focussing is necessarily monochromatic

of the crystal thus does not simply produce to a further increase in the scattered beam but may, on the contrary, redirect the neutrons into transmission. This effect is called primary extinction. Primary extinction is responsible for the finite wavelength acceptance [29] of a perfect crystal ($\Delta d = 0$) for an ideally collimated beam $\Delta\theta = 0$, which is called the Darwin width.[20] In the case of silicon, the *Darwin width* amounts to a few seconds of arc. In the same way as the angular acceptance is finite for an ideal monochromatic beam, the monochromaticity of a backscattered beam is finite.

It is evident that crystal monochromators work best for neutrons with wavelengths in the vicinity of the lattice distances, allowing for reasonably large Bragg angles. In particular for long wavelength neutrons ($\lambda > 6$ Å), large d-spacings are required in order to maintain a reasonable resolution. Such crystals of good reflectivities are not available naturally. We, therefore, have to use artificially layered materials or the time-of-flight technique. A similar problem is encountered for very short wavelengths where reflectivities for small d-spacings decrease rapidly, among other reasons, because of the thermal vibrations of the atoms. Here a cooling of the monochromator can be an efficient means of increasing the diffracted intensity.

3.3.6 Time-of-Flight Filters

If the dimensions of the slits that the neutron beam encounters along its path are large compared to the neutron wavelength, then the beam propagation may be treated *ballistically*, that is, as the ensemble of trajectories of non-interacting classical particles. Apart from the specificities related to the finite mass of the neutron, this treatment is equivalent to the ray optics of electromagnetic radiation. A classical particle of velocity v spends a well-defined time t traveling a distance L. By measuring the time-of-flight t, we can determine v and thus the energy of the particle. In a beam with no possibility of labeling the individual particles, this technique works only if all neutrons have the same starting time, that is, if the beam is pulsed. Pulsing can be produced at the source, which is the most economic way, as right from the start unwanted neutrons are not produced. In the case of continuous sources, the pulsing can be achieved via turning devices that open the beam for a limited amount of time Δt, eliminating all the neutrons produced outside this time window. According to whether the pulsing is done (i) via collimators turning about an axis perpendicular to the beam or by (ii) absorbing disks with transparent slits rotating about an axis parallel to the beam, we speak of *Fermi* [30] or *disk choppers*, respectively (see Fig. 3.10).

We will now derive some useful relations for neutron time-of-flight spectroscopy. The energy of a free neutron is related to its classical speed $\vec{v}$ via

[20] This effect cannot be described by the Bragg equation, as it was derived on the assumption of an infinitely large homogeneously illuminated scattering volume.

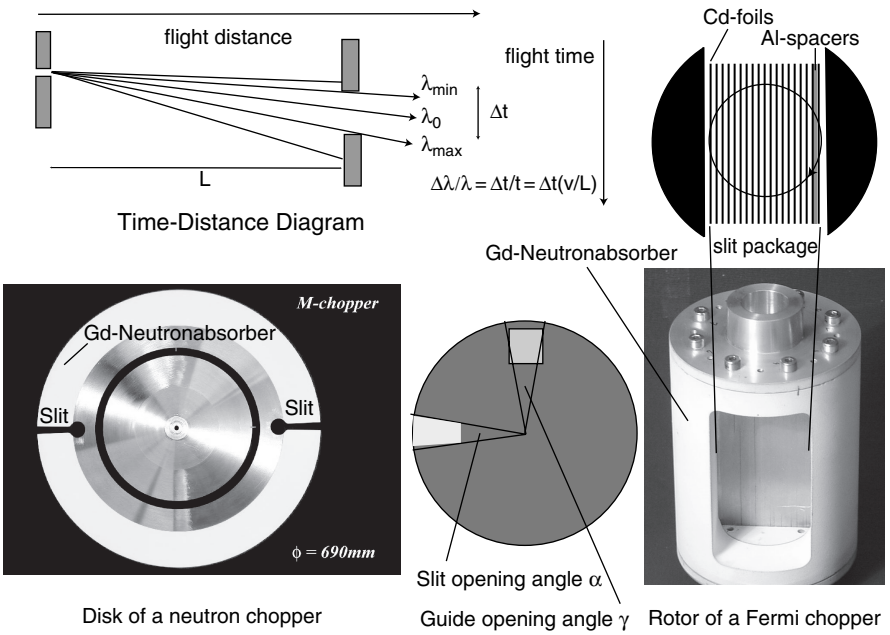

Fig. 3.10 Filtering wavelength bands from a neutron beam via the time-of-flight method. A pulse of neutrons with a distribution in velocity $v = \frac{h}{m\lambda}$ separates in time. Only those neutrons arriving within the time interval Δt at the chopper are transmitted. The relative wavelength resolution $\Delta\lambda/\lambda$ is proportional to the opening time Δt divided by the flight time t. The pulsing is achieved either by the source or by mechanical devices, the so-called neutron choppers. Disk choppers turn with their axis of rotation parallel to the beam. Open slits alternate with absorbing sections. For a disk with an opening angle α corresponding to the angular opening γ of the guide, the transmission as a function of time is triangular. For $\alpha > \gamma$ we get a trapezoid. The FWHM is given for single choppers to good approximation by $\tau = (\alpha + \gamma)/2\omega$, with ω denoting the angular speed of the chopper. If we work with a so-called counter-rotating chopper, that is, with two chopper disks right next to each other and turning in opposite direction, then the opening time is halved ($\tau = \alpha/2\omega$). Fermi-choppers have the axis of rotation perpendicular to the beam. The chopping is achieved via a rotating collimator made of absorbing sheets alternating with transparent spacers. The opening time is defined by the divergence α of the slip pack. Its FWHM is given as $\tau = \alpha/\omega$

$$E = \frac{1}{2}mv^2 = \frac{\hbar^2 k^2}{2m}, \qquad k = \frac{2\pi}{\lambda}. \tag{3.41}$$

$\vec{k}$ is the wavevector of the matter wave associated with the free neutron of well-defined linear momentum $\vec{p} = \hbar\vec{k}$. This means (see Eq. (3.1)) that neutrons of a few Å wavelength possess an energy of a few meV, which corresponds to typical excitations in solids. This perfect match of microscopic length and energy scales with the wavelength and energy of the neutron is one of the many reasons why neutrons are an ideal tool for the investigation of microscopic processes. From the instrument design point of view, the velocities are more important than the energies as they determine the opening times required for filtering the energies.

$$v = \frac{\hbar k}{m} = \frac{h}{m\lambda} = \frac{6.6261 \cdot 10^{-34}\mathrm{Js}}{1.6749 \cdot 10^{-27}\mathrm{kg}} = \frac{3956\frac{\mathrm{m}}{\mathrm{s}}}{\lambda[\mathrm{Å}]}. \tag{3.42}$$

Neutrons of $\lambda = 4\,\mathrm{Å}$ thus have a speed of about $1\,\mathrm{km\,s^{-1}}$. The maximum in the energy distribution of a thermal moderator at room temperature ($T = 293\,\mathrm{K}$) corresponds to neutrons of speed 2200 m/s. The fundamental equation governing time-of-flight spectroscopy relates the travel time t over a distance L to the neutron wavelength λ:

$$t = \alpha L\lambda\ ,\ \alpha = m_\mathrm{n}/h = 252.77\mu\mathrm{s}/(\mathrm{Å m}). \tag{3.43}$$

A pulsed beam of width τ that has travelled down a distance L will have at any time t a relative wavelength spread of

$$\frac{\Delta\lambda}{\lambda} = \frac{\tau}{t}. \tag{3.44}$$

If we take $L = 10\,\mathrm{m}$ and $v_0 = 1000$ m/s, we can achieve a 1% wavelength resolution for a pulse width of $\tau = 100\,\mu\mathrm{s}$. To produce such a pulse for typical guide cross sections, we need a device turning at 6000 rpm, which is a reasonable frequency for cyclic mechanical motion.[21] The shape of the distribution $p(\lambda)$ after the filter depends on the transmission T of the opening mechanism as a function of time. For mechanical devices like disk choppers, the transmission T corresponds at any time t to the folding of the slit cross section with the guide cross section (see Fig 3.10). For rectangular slits in front of rectangular guides $T(t)$ is a trapezoid, which becomes a triangle if the slit has the same width as the guide. Single disks open and close at the edge of the guide. Counter-rotating disks open and close the passage for the beam in the center of the guide. $T(t)$ has for mechanical devices well-defined cut-offs. Statistical contributions like fluctuating chopper phases add small Gaussian contributions. This clean resolution without wings is one of the main advantages of a time-of-flight filter.

In contrast to wavelength dispersive filters, time-of-flight filters do not introduce a correlation between angle and wavelength. In particular, they do not break left–right symmetry. This can be very advantageous when working with large detector arrays (see Fig. 3.16). They, however, introduce by definition a correlation between wavelength and time. As time is taken with respect to the opening of the choppers, this leads to a correlation of wavelength and position over the transmitted beam cross section.

The energy filtering performance depends strongly on the wavelength. From Eqs. (3.41 and 3.42) we deduce that the energy uncertainty ΔE connected with a time uncertainty Δt goes with the third inverse power of the wavelength:

[21] The task of pulsing the beam would be considerably more difficult, if we were dealing with lighter particles (e.g., electrons) of the same kinetic energy and spread out over similar guide cross sections.

$$\Delta E = \frac{h^3}{m^2\lambda^3}\frac{\Delta t}{L}. \tag{3.45}$$

From an energy resolution point of view, it is thus recommended to work with the longest wavelength possible.

For a pulses source and a particular moderator, the pulse width is given. In that case we have to invert the above argument. To obtain a specific wavelength resolution from a given pulse width τ, we need a certain flight time t. This is no problem for a single pulse provided we can transport the neutrons efficiently over large distances, such as with the help of ballistic guides. For a sequence of pulses, we are confronted with the *frame overlap* problem. If we start out with a very broad spectrum of wavelengths, then the fast neutrons of a given pulse will sooner or later take over the slower ones of previous pulses. This frame overlap will pollute the characteristics of a time-of-flight filter. The problem can be overcome by limiting the acceptable wavelength band, by adding supplementary choppers to the time-of-flight filter. If this is not possible, for example, because the full wavelength band is needed for the experiment, then the only solution is increasing the time between the pulses or in reducing the original pulse width. The ration τ/t thus can be regarded as the intrinsic wavelength resolution capability of the filter [18]. In the case of a pulsed source, it is identical to the *duty-cycle* of the source, that is, to the percentage of time the source is on. A long pulse source with a low repetition rate thus has a similar intrinsic wavelength resolution as a short pulse source with a higher repletion rate but equal duty cycle.

To obtain a monochromatic pulsed beam, it is sufficient to place a second so-called *monochromating chopper* at a distance L_{pm} downstream from the *pulse creating chopper*. This chopper cuts a certain wavelength band from the incoming spectrum, producing a monochromatic pulsed beam. If the neutron source itself is pulsed with an adapted pulse length, the source can in principle take over the role of the pulsing chopper. However, in practice it turns out that a pulse-shaping chopper is still needed in most cases to define a perfect pulse shape without wings.

3.3.7 Velocity Selectors

We have seen that time-of-flight filters allow neutrons to be sorted in time according to their energy. Monochromatic pulsed beams are obtained by selecting a slice of the sorted energy spectrum. In many cases the correlation of energy with time is not required; that is, we are completely satisfied with a continuous but coarsely monochromatized beam. This can be achieved via *velocity selectors* [31–33]. In a velocity selector the neutrons are sorted into helical channels cut into a cylinder that rotates with a speed ω (see Fig. 3.11). Neutrons traveling parallel to the axis of rotation of the cylinder will keep a constant distance from the channel walls provided they have a velocity given by

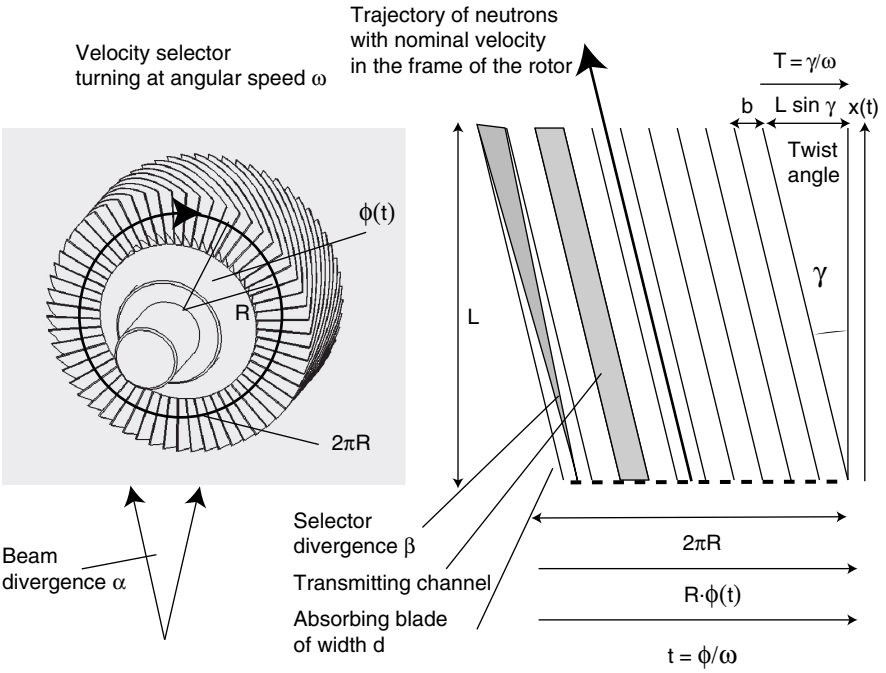

Fig. 3.11 Velocity selectors. The diagram to the right is obtained by rolling the selector at a given radius R onto a flat surface. This distance–distance diagram can be mapped onto a time–distance diagram $x(t)$ for the neutron. The time t corresponds to the angle Φ covered during the period t by the selector. Neutrons traveling parallel to the axis of rotation of the cylinder will keep a constant distance from the channel walls, provided they travel the distance L during the time T, which is necessary to change the orientation of the selector by the angle γ. This leads to Eq. (3.46). The finite width d of the blades leads to transmission losses. Neutrons traveling parallel to the axis of rotation but with different velocity can pass the detector, provided their trajectories fall into the divergence of the selector defined by the angle $\beta \approx b\cos\gamma/L$. If the neutrons impinge onto the selector with a divergence α, this leads to further broadening of the wavelength band. Both transmission and resolution depend on the distance from the center of the rotor; that is, they change over the height of the beam (Drawing of velocity selector courtesy of Lukas Födinger.)

$$v = \frac{L}{\gamma}\omega, \tag{3.46}$$

that is, a wavelength

$$\lambda[\text{Å}] = \frac{h}{mv} = \frac{h\gamma}{mL\omega} = 3956\frac{\gamma}{\omega[\text{s}^{-1}]L[\text{m}]}, \tag{3.47}$$

with γ denoting the pitch or twist angle of the helix (the phase change between the two faces of the rotor of length L). Thus a 30-cm long velocity selector running at 10,000 rpm and featuring a twist angle of 45° would have maximum transmission for neutrons of about 10 Å. A velocity selector can be described as a cascade of an

infinite number of disk choppers [34]. As neutrons are fully confined to one channel, there is no cross-talk between the channels as in the case of a finite chopper cascade. The selector can thus work quasi-continuously; that is, the channels can cover the whole volume of the cylinder, one lying next to the other along the circumference. A neutron missing one channel will immediately find the following one so that there is no loss in flux apart from that unavoidable due to the finite thickness d of the channel walls. As can be deduced from the diagram of Fig. 3.11, a given channel is open for a time $\tau = b/(2\pi \cdot R \cdot \omega)$. As the flight path L for a parallel beam is given by the length of the selector, neutrons will path the selector if they are faster than $v_0 - L/\tau$ or slower than $v_0 + L/\tau$. The shape of the distribution $p(\lambda)$ after the selector is triangular and

$$\Delta\lambda = \lambda \frac{b}{L \sin\gamma} = \frac{\beta}{\tan\gamma}, \tag{3.48}$$

gives the FWHM of this triangle. The triangular shape can be understood by considering that neutrons with the nominal speed will be transmitted over the full width of the channels, while the extreme cases (the neutrons at the very fast or very slow end) are transmitted only if they enter the channels on the left and exit on the right or vice versa. In between, the transmission decreases linearly on both sides of the maximum. The argument is similar to the one used for disk choppers. In the case of a divergent beam, the divergence α has to be added quadratically to β in Eq. (3.48), decreasing the wavelength resolution of the chopper further.

$$\frac{\Delta\lambda}{\lambda} = \frac{\sqrt{\beta^2 + \alpha^2}}{\tan\gamma}. \tag{3.49}$$

Velocity selectors are used mainly in applications that require a rather relaxed resolution. To reach a 10% wavelength resolution with a selector of the above mentioned characteristics, we require an opening of about 4.5°. This selector thus has to feature at least 80 channels, that is, 80 blades separating the different compartments. For a 1% resolution we would require 800 blades, which is not only technically impossible but also equally would lead to a selector with hardly any transmission.

3.4 Instruments

We have reviewed in the last section the most important devices for shaping and filtering non-polarized neutron beams. These devices are the necessary and sufficient elements to design the most common non-polarized neutron spectrometers. We will illustrate this fact by presenting a number of instrument classes that allow to determine the scattering function $S(\vec{Q}, \hbar\omega)$ under various conditions. In the last part of this section we will deal with the spin-echo technique. It has the peculiarity of determining the time Fourier transform $I(\vec{Q}, t)$ of the scattering function by encoding of the velocity change of the neutrons in the beam polarization. Only at this point

we will be obliged to add polarization manipulation devices to our instrumentation tool box.

3.4.1 Three-Axis Spectrometers

The three-axis spectrometer (see Fig. 3.12) can be considered the mother of all crystal spectrometers [25]. It allows both the momentum $\vec{Q} = \vec{k}_i - \vec{k}_f$ and the energy transfer $\hbar\omega = E_i - E_f$ of the neutrons to be determined. This is achieved by shaping monochromatic beams of neutrons before and after the scattering event with the help of Bragg scattering from crystals (see Section 3.35), called *monochromator* and

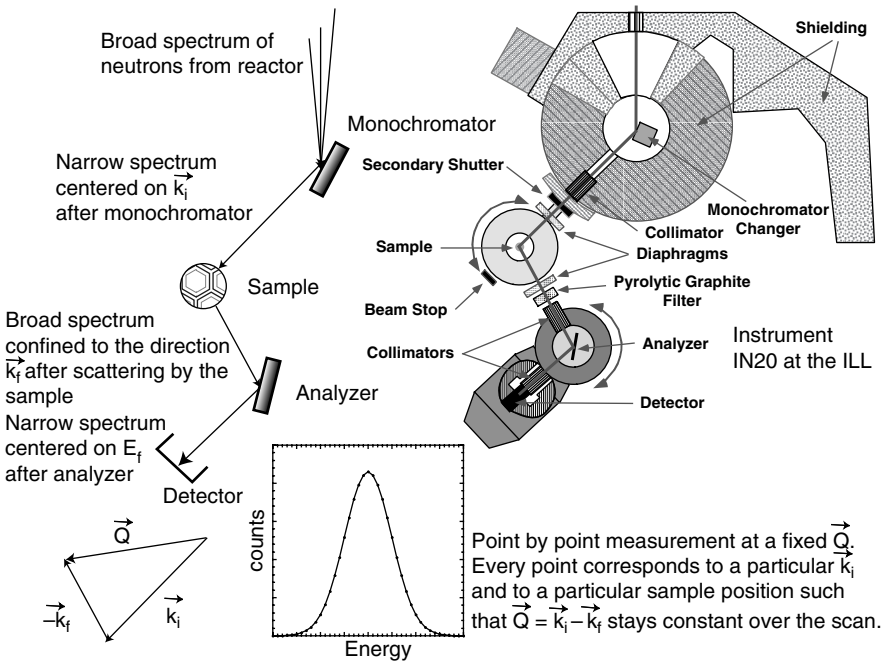

Fig. 3.12 Schematics of a three-axis spectrometer. During the point-by-point measurement, $\vec{k}_i$ (Bragg angle of the monochromator) and $\vec{k}_f$ (angular position of the analyzer as well as Bragg-angle of the analyzer) are permanently readjusted such as to follow a precise trajectory in $\vec{Q} = \vec{k}_i - \vec{k}_f$ and $\hbar\omega = E_i - E_f$. The sample orientation adapts to the changing spectrometer configurations in such a way that the $(Q, \hbar\omega)$ setting of the spectrometer is mapped onto a precise $(Q, \hbar\omega)$ point of the sample's reciprocal space. The resolution of the spectrometer is determined by the divergence of the respective beams as well as by the mosaic of the monochromator and analyzer crystals. Due to the breaking of right-left symmetry by Bragg scattering, configurations with alternating sense of scattering at monochromator, sample and analyzer so-called *W-configuration* (shown here is a right–left–right arrangement) offer better resolutions than so-called *U-configurations*. In many cases it is sufficient to keep a rather tight energy resolution. The relaxed $\vec{Q}$-resolution can be attained by curving the crystals and working with diaphragms but no collimators. This leads to appreciable gains in intensity particularly important for small samples

analyzer, respectively. Typical crystals are graphite, copper or silicon. The primary and secondary beams are characterized by well-defined wavevector distributions $p(\vec{k}_i)$ and $p(\vec{k}_f)$.

By using focusing geometries, monochromators and analyzers not only filter energy bands but equally concentrate the beam spatially onto rather small sample volumes. This naturally comes at the price of increased beam divergence and thus lower resolution in $\vec{Q}$. The analyzer turns around the sample position to allow for varying momentum transfer $\vec{Q} = \vec{k}_i - \vec{k}_f$. In the classical form only one analyzer crystal is used, while multi-analyzer spectrometers allow to monitor simultaneously a whole array of $\vec{k}_f$-values [35]. The sample is normally of single crystalline form and its orientation in the classical mode of operation is permanently readjusted such that the momentum transfer of the neutrons coincides with a particular point in the $(\vec{Q}, \hbar\omega)$ space of the sample. In this way the scattering function $S(\vec{Q}, \hbar\omega)$—once the data corrected for resolution—can be determined in a point-by-point mapping.

It can be shown [16, 36] that for mosaic crystals the resolution (see Eq. 3.22) of a three-axis spectrometer is given by

$$R(\vec{Q}_0 + \Delta\vec{Q}, \hbar(\omega_0 + \Delta\omega)) = R(\vec{Q}_0, \hbar\omega_0) \exp\left\{-\frac{1}{2}\sum_{k=1}^{4}\sum_{l=1}^{4} M_{kl} X_k X_l\right\}, \quad (3.50)$$

with $X_1 = \Delta Q_x$, $X_2 = \Delta Q_y$, $X_3 = \Delta Q_z$, and $X_4 = \hbar\Delta\omega$. The (4×4)-matrix (M_{kl}) is a complex function of the beam divergences and mosaicities of the crystals. It fully describes the resolution properties of a particular instrument set-up. The nice feature about Eq. (3.50) is that despite the complexity of (M_{kl}) any straight cut of the resolution function through $(\vec{Q}_0, \hbar\omega_0)$ leads to a Gaussian function.[22] The surfaces in $(\vec{Q}, \omega)$ space, for which the resolution function, that is, for which

$$\sum_{k=1}^{4}\sum_{l=1}^{4} M_{kl} X_k X_l \quad (3.51)$$

is constant are *ellipsoids* in four-dimensional space. When graphically illustrating the ellipsoids, one normally uses the line that corresponds to a drop in intensity of 50%. In the case of scans through dispersive single crystal excitations like phonons, the orientation of the ellipsoid with respect to the dispersion relation is important. If at a given $(\vec{Q}, \hbar\omega)$ point the long axis of the ellipsoid is aligned parallel to the dispersion $\hbar\omega(\vec{q})$, the resolution in energy is better (focusing configuration) than in the case of a perpendicular orientation (anti-focusing configuration).[23]

Using a large variety of crystals for both monochromator and analyzer on cold, thermal and hot sources energy transfers from 0 up to 200 meV can be covered

[22] This relies on the fact that the transmission of both collimators and crystals is a very good approximation Gaussian (see Sections 3.3.5 and 3.3.4, as well as [36]).

[23] We have used the notation $\vec{q} = \vec{Q} - \vec{\tau}_{\mathrm{hkl}}$ with $\vec{\tau}_{\mathrm{hkl}}$ indicating the closest reciprocal lattice vector.

with a relative resolution of a few percent. The choice of the instrument configuration is motivated by the requirement to close a scattering triangle for a particular $(\vec{Q}_0, \hbar\omega_0)$ point, while retaining sufficient resolution in both $\vec{Q}$ and $\hbar\omega$ to determine the structure of $S(\vec{Q}, \hbar\omega)$ in the vicinity of $(\vec{Q}_0, \hbar\omega_0)$. Naturally, all the effort is in vain unless the dynamic range and resolution are matched by sufficient intensity and signal-to-noise allowing for satisfactory data statistics within reasonable measuring time.

One problem of three-axis spectrometers is higher-order Bragg scattering. Apart from the nominal energy E_i, the monochromator equally transmits $E_n = n^2 E_i, n = 2, 3, \ldots$, and the same holds for the analyzer. This can lead to *spurious scattering*. Elastic scattering may, for example, spuriously appear in the inelastic channels when the relation $n_1^2 E_i = n_2^2 E_f, n_i, n_f = 1, 2, 3, \ldots$ is fulfilled. The probability of such events is particularly high when $E_i >> E_f$. The effect can be reduced by using a velocity selector or adapted energy filters. An often used low-pass filter is Be-powder [37]. It deflects all neutrons with wavelength shorter than 3.96 Å, that is, with energies higher than 5.2 meV into Debye-Scherrer rings (see Section 3.4.4). Longer-wavelength neutrons do not meet the Bragg condition even in backscattering and are thus transmitted unless they are scattered inelastically by crystal vibrations. To reduce the inelastic attenuation of the beam, Be-filters are cooled to liquid nitrogen temperatures.

3.4.2 Backscattering Spectrometers

We have seen (Eq. (3.37)) that a crystal monochromator has its highest resolution in backscattering, that is, for Bragg angles of 90°. A backscattering spectrometer is a three-axis spectrometer where both the monochromator and the analyzer work in backscattering geometry [38]. We can deduce from Fig. 3.13 the lengthening of the wave-vector when going out of backscattering by an angle ϵ for the value of highest divergence $\Delta\theta/2$ as

$$\Delta k = k_0 \left(\frac{1}{\cos\left(\epsilon + \frac{\theta}{2}\right)} - 1 + \frac{\Delta\tau}{\tau} \right), \tag{3.52}$$

which for ideal backscattering and reasonably small divergences leads to

$$\frac{\Delta k}{k_0} = \frac{1}{8}\Delta\theta^2. \tag{3.53}$$

$\Delta\tau = 2\pi/\Delta d$ gives the spread in lattice constant due to strain and other crystal imperfections. As we have already mentioned in Section 3.3, even perfect crystals do have a finite band width in backscattering. Therefore, the energy resolution cannot be better than

$$\frac{\Delta E}{E} = 2\left[\frac{1}{8}\Delta\theta^2 + \frac{16\pi N_c |F_{hkl}|}{|\vec{G}_{hkl}|^2}\right]. \tag{3.54}$$

For reflection from perfect Si(111) planes ($\lambda = 6.27\text{Å} \approx 2\pi\,\text{Å}$, $E = 2.08\,\text{meV}$) and a beam with the divergence arising at this λ from a Ni-coated guide ($\Delta\theta = 1.25^\circ = 0.02\,\text{rad}$), we get $\Delta E = (0.24{+}0.08)\,\mu\text{eV}$. The contribution from the beam divergence is thus three times more important than that due to primary extinction. To retain a reasonable neutron flux it is not recommended to decrease the divergence in order to fully match the two terms. To the contrary, in practice slightly imperfect crystals are accepted leading to an overall resolution (monochromator plus analyzer) of a bit less than 1 μeV.[24]

As both the monochromator and the analyzer are set in backscattering, the energy transfer is fixed. If both the analyzer and detector use the same reflection, then the energy transfer is zero and only neutrons falling into the resolution window (about 1 μeV for Si111 reflections) will be counted. This allows determining the strictly, elastic scattering of the sample. If registered as a function of temperature, the drop of the elastic intensity signals the onset of motion faster than a few nanoseconds, e.g., because the sample starts melting. This kind of instrument operation is called *fixed* (energy) *window scan*.

The whole idea of backscattering spectroscopy is based on the fact that the wavelength does to first order not depend on the scattering angle. It is, thus excluded to scan the energy in the classical three-axis mode by turning the monochromator. This is best demonstrated by a simple calculation. If we want to achieve a dynamic range of about 10 times the resolution, then we have to change the incoming energy by ±10 μeV. Using the Bragg equation this leads to a Bragg angle of $\theta = 86^\circ$ for Si111. At this angle we would, however, already have a linear contribution to the resolution (see Eq. (3.37)) of $\Delta E = 5$ μeV, i.e., 50% of the dynamic range, which is not acceptable. As a variation of the angle is excluded we are left with the possibility of acting upon the lattice spacing d. It can be changed either thermally or by moving the crystal parallel to the neutron trajectory (Doppler broadening). From basic considerations of energy and momentum conservation, the *Doppler broadening* induced by a crystal with speed v_D is given as

$$\Delta E = 2E\frac{v_\text{D}}{v} + O\left(\left(\frac{v_\text{D}}{v}\right)^2\right). \tag{3.55}$$

If we take $\lambda = 6.27\,\text{Å}$ and a Doppler velocity of 5 m/s, then (see Eq. (3.42)) $v_\text{D}/v \approx 1.6{\cdot}10^{-2}$, that is, we achieve an energy transfer of about $\pm 30\mu$eV (provided that the deflector is capable of transmitting such a 3% wavelength band). Thermal expansion in crystalline materials is of the order of $\frac{\Delta d}{d} \approx 10^{-5}$ per K. By heating

[24] On IN16 at the ILL this 1 μeV resolution is accompanied by a Gaussian profile of $p(\hbar\omega)$. This is not a trivial fact as the Darwin distribution arising from primary extinction is not Gaussian.

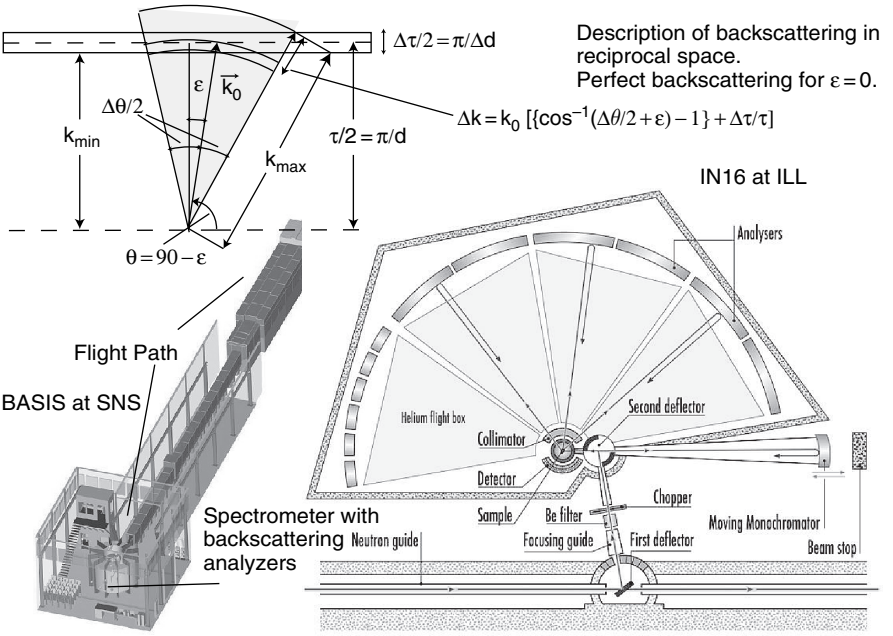

Fig. 3.13 Backscattering spectrometers. IN16 is the classical type of a backscattering spectrometer. The neutrons from the guide are deflected twice before they hit the monochromator (at a guide end position the first deflector would not be necessary). A narrow wavelength band $\Delta\lambda_i$ comes back from the monochromator to the sample. The second graphite (002) deflector is mounted as two reflecting quarter circle segments on a chopper. This insures that the monochromatic neutrons returning from the Doppler-driven monochromator can pass to the sample by the remaining two open segments of the chopper. The sample is placed directly behind this chopper. The background arising during the opening of the graphite deflector is suppressed by an additional chopper. Higher-order reflections from the graphite are cut off by a cooled beryllium filter. From the sample the neutrons are scattered into the analyzers (The detectors placed close to the sample do not collect data at that moment.). The analyzers select a narrow wavelength band $\Delta\lambda_f$ that is transmitted back through the sample into the detector. As the flux is low, large spherical analyzers are used leading to a rather poor Q-resolution. The incoming energy is varied by moving the monochomator parallel to the neutron trajectory. The neutrons experience positive and negative Doppler shifts proportional to the monochromator speed (Eq. (3.55)). In the case of a pulsed source instrument like BASIS at SNS backscattering is used only for the energy filtering after the sample. The incoming energy is selected using the time-of-flight technique. As an energy resolution close to that of the backscattering analyzers is required, it is necessary to use a short pulse in conjunction with a long flight path. At SNS this is achieved at 84 m using the poisoned moderator $\Delta t \approx 50 - \mu$s at 6 Å. The diagram shows backscattering in the space of the neutron wave-vectors. τ is perpendicular to the surface and of length $2\pi/d$. Primary extinction or crystal imperfections lead to a relative wavelength uncertainty ($\frac{\Delta\tau}{\tau} = 1.86 \times 10^{-5}$ for perfect Si 111), which can be considered a radial mosaic

a CaF_2 ($\lambda = 6.307\,\text{Å}$) crystal (as used on the backscattering instrument IN13 at the ILL) from 77 to 700 K, the energy can be varied by $\frac{\Delta E}{E} = 2\frac{\Delta d}{d} \approx 3.3\%$. The heating of the monochromator is a slow process. The result of the scan is thus only available after hours of data accumulation, while in the case of the Doppler drive the spectrum is collected simultaneously.

3.4.3 Time-of-Flight Spectrometers

The instruments discussed so far filter the energy of the neutrons using Bragg optics. While this works very well in the thermal range, the method has limitations for very hot (loss in reflectivity of the crystal) and very cold neutrons (insufficient d-spacing) as we have seen in Section 3.3.5. In addition, an array of many crystals is geometrically cumbersome if a large solid angle Ω of scattered neutrons has to be analyzed. The time-of-flight filter discussed in Section 3.3.6 has the advantage that it works for any wavelength on the condition that suitable mechanical devices for closing and opening the beam are available. Time-of-flight spectrometers can be grouped into two main classes: (i) *direct* and (ii) *indirect geometry spectrometers*. Direct geometry spectrometers work with a pulsed monochromatic beam at the sample. The monochromatization can be achieved with a crystal followed by a Fermi-chopper taking care of the pulsing. In that case the primary spectrometer resembles very much that of a three-axis instrument. The energy after the scattering is analyzed by measuring the time it takes the neutron to travel the known distance L_{sd} from the sample to the detector. In this way we obtain a spectrum of intensity $I(t)$ with $E_f(t) = \frac{m}{2}\frac{L_{sd}^2}{t^2}$ for every detector pixel (see Fig. 3.14). As the neutrons arriving from the monochromator at the Fermi-chopper possess a very strong correlation of wavelength and angle, the speed of rotation of the chopper has a strong influence on the resolution [39]. If chosen correctly, then the slower neutrons pass the Fermi-chopper first catching up with the faster ones at the detector. This so-called *time-focusing* naturally depends on the energy transfer the neutrons experience at the sample. Faster chopper rotation leads to a fulfillment of the focusing condition at higher energies in up-scattering (neutron energy gain).

When working with very cold neutrons, both the crystal monochromator and the Fermi-chopper run into performance problems. It is then necessary to replace the primary spectrometer by a cascade of disk choppers. The chopper closest to the source creates pulses.[25] A second chopper is placed as close to the sample as possible. It performs the energy filtering using the fact that neutrons will disperse along the path from the pulsing to the monochromating chopper. The intensity at the detector of such a spectrometer is proportional to the product $\tau_p \cdot \tau_m$ of the opening times of the pulsing and monochromating choppers [40, 41].

[25] In the case of a pulsed source, this function can in principle be assured by the source itself. In most cases it is, however still necessary to shape the pulse.

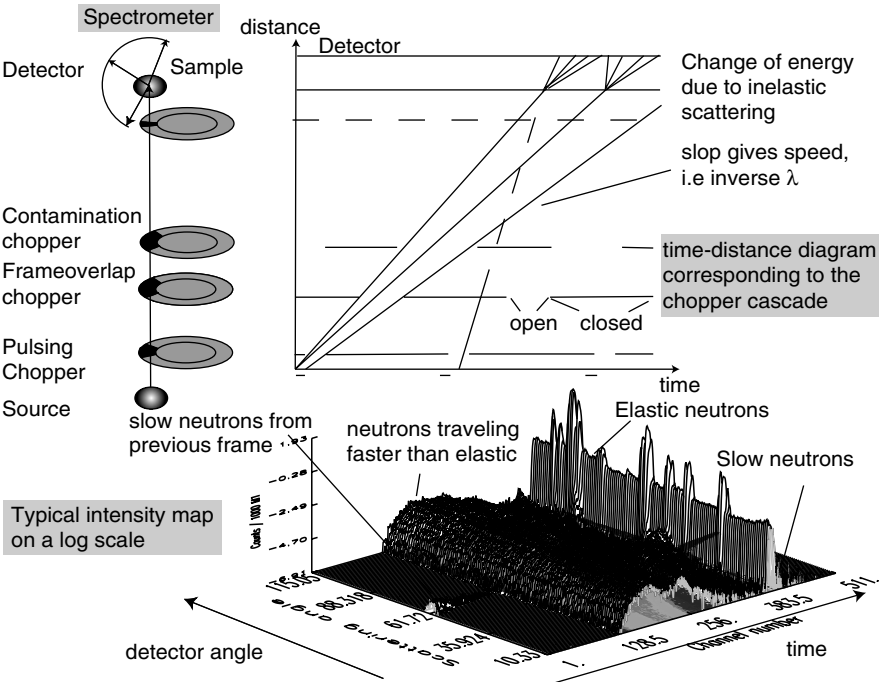

Fig. 3.14 Schematic lay-out of a generic chopper spectrometer. The pulsed source—or in the case of a continuous source the pulsing chopper—produces bursts of polychromatic neutrons. These neutrons disperse as they travel to the sample. Within the resolution of the instrument a particular neutron velocity is selected by the monochromating chopper. Additional choppers are necessary to avoid the contamination of the beam by neutrons originating from other source pulses. If the frequency of the pulses is sufficiently low, like in the case of a long-pulse spallation source, several wavelength packages can be selected from one source pulse. This scheme of *repetition rate multiplication* [6, 42] allows using the full time between source pulses for efficient data collection in time-of–flight spectroscopy. A good overview of the beam trajectories can be obtained via a time–distance diagram. The data acquisition covers the accessible $(\vec{Q}, \hbar\omega)$-range simultaneously. Every detector pixel described by angles (θ, Φ) is associated with a spectrum $I(t)$. Neutrons having gained energy at the sample (up-scattering) arrive prior to those having been scattered elastically, while the slower ones follow later. Neutrons slowed down too strongly by the scattering from the sample will be detected simultaneously with the fast ones from the successive pulse. This frame overlap can be reduced at the expense of intensity by increasing the time between pulses using a suppressor or frame-overlap chopper

The energy resolution of a time-of-flight spectrometer is determined by the accuracy of measuring the flight time and flight path. The width in time Δt of a pulsed beam when arriving at the detector can be derived directly from the time–distance diagram using purely geometric arguments. Converting the time uncertainty into an apparent energy width ΔE on the basis of Eq. (3.45) we obtain

$$\Delta E[meV] = 0.6472 \frac{\left[\Delta t_{\mathrm{p}}^2 + \Delta t_{\mathrm{m}}^2 + \Delta t_{\mathrm{l}}^2\right]^{1/2}}{\lambda_f^3 L_{\mathrm{pm}} \cdot L_{\mathrm{sd}}} \tag{3.56}$$

with

$$\Delta t_{\mathrm{p}} = \tau_{\mathrm{p}} \left(L_{\mathrm{ms}} + L_{\mathrm{sd}} \frac{\lambda_f^3}{\lambda_i^3} \right) \tag{3.57}$$

$$\Delta t_m = \tau_{\mathrm{m}} \left(L_{\mathrm{pm}} + L_{\mathrm{ms}} + L_{\mathrm{sd}} \frac{\lambda_f^3}{\lambda_i^3} \right) \tag{3.58}$$

$$\Delta t_{\mathrm{l}} = L_{\mathrm{pm}} \cdot \lambda \cdot \alpha \cdot \Delta L. \tag{3.59}$$

L_{pm}, L_{ms}, and L_{sd} denote the distance from the pulsing to the monochromating chopper, from the monochromating chopper to the sample, and from the sample to the detector, respectively. The equation simplifies considerably in the case of elastic scattering, that is, for $\lambda_i = \lambda_f$. The first contribution Δt_{p} describes the spreading of the initial pulse τ_{p} at the detector in the case of a hypothetical infinitely sharp opening of the monochromating chopper. The second contribution Δt_{m} arises from the spread that an infinitely sharp pulse from the pulsing chopper (or source) experiences at the detector due to the finite opening time of the monochromating chopper τ_{m}. The flight path uncertainties ΔL include finite sample and detector size. They translate into a spread of arrival times, which is not related to differences in velocity.

Using Eq. (3.44) we get a time uncertainty of about 25 μs for a typical value of $\Delta L = 20\,\mathrm{mm}$ and $\lambda = 5\,\text{Å}$. This sets the scale for the chopper openings, which should produce time uncertainties in the same range to achieve balanced resolution contributions to Eq. (3.56).

Indirect geometry time-of-flight spectrometers use crystal analyzers to determine the final energy. The incoming beam is energy dispersive, that is, neutrons arrive with energies $E_i(t) = \frac{m}{2} L_{\mathrm{ps}}^2 / t^2$ at the sample with L_{ps} denoting the distance to the pulse creating device. The intensity measured in the detector reflects the time dependence of the incoming spectrum. Indirect geometry spectrometers are particularly useful when large energy transfers are to be investigated with high resolution like in the case of vibrational spectroscopy. A typical example is TOSCA at ISIS. The resolution of the secondary spectrometer being high and constant the overall resolution is determined mainly by the length of the primary flight path from the pulsing chopper to the sample. Time-of-flight spectrometers give access to energy transfers up to several hundred meV. The best resolution of about 10 μeV is obtained with disk chopper spectrometers at long wavelengths. Time-of-flight spectrometers thus connect in energy to the dynamic range of backscattering spectrometers, however,

with a reduced Q-range. At higher energies the resolution varies usually between 2% (high resolution) and 5% (high intensity).

A particular type of indirect time-of-flight spectrometer is that using the crystal analyzers in backscattering geometry (see Section 3.4.2). The time uncertainty $\Delta t/t$ has to match the resolution $\Delta\lambda/\lambda \approx 0.25 \cdot 10^{-3}$ of backscattering. This implies long flight times and short pulses. A typical example is the spectrometer BASIS at SNS (see Fig. 3.13) . It combines a flight path of 84 m with a short 50 μs pulse from the poisoned moderator leading at 6 Å to a theoretical $\Delta t/t \approx 0.5 \cdot 10^{-3}$. The advantage of this time-of-flight backscattering spectrometer with respect to the classical three-axis type is the large dynamical range due to the fact that the incoming energy varies simply as a function of time without the need for a Doppler drive or heated monochromator. In practice it has, however, difficulties in attaining the ultimate backscattering energy resolution.

3.4.4 Fixed-Wavelength Diffractometers

If we use a three-axis spectrometer without the analyzer, then we will integrate the signal over all final energies, that is, we determine—after corrections for resolution and integration over the solid angle Ω spanned by the detector area—the diffraction pattern [43]

$$I(2\theta) = \int_{\Omega} \frac{\mathrm{d}\sigma}{\mathrm{d}\Omega}\mathrm{d}\Omega = \int_{\Omega} \mathrm{d}\Omega \int \frac{\mathrm{d}^2\sigma}{\mathrm{d}\Omega \mathrm{d}E_f} dE_f. \tag{3.60}$$

The structural information of the sample, that is, the correlation of the atomic positions at any time t is given by the energy integrated scattering function

$$S(\vec{Q}) = \hbar \int S(\vec{Q}, \hbar\omega)\mathrm{d}\omega. \tag{3.61}$$

Both expressions could be directly converted into each other if the integration over energy done by the spectrometer was (i) complete and (ii) not mixing inelastic intensity corresponding to various $\vec{Q}$ values in the same detector pixel. In general, the corrections due to these deficiencies in the energy integration can be handled and thus the structural information can be fully retrieved from the diffraction pattern [44].

If the sample is a single crystal, the scattering will consist of Bragg peaks. The experimental task consist in measuring the Bragg intensities (see Eq. (3.39)) with sufficient accuracy to extract the structure factors $|F_{hkl}|$ corresponding to the (hkl) lattice planes. In a single counter mode this is achieved by scanning the intensity as a function of $(\omega, 2\omega)$, with ω denoting the rotation of the crystal in the equatorial plane of the spectrometer and 2ω the concomitant detector rotation. The orientation of the crystal is assured by Eulerian cradles that allow attaining arbitrary

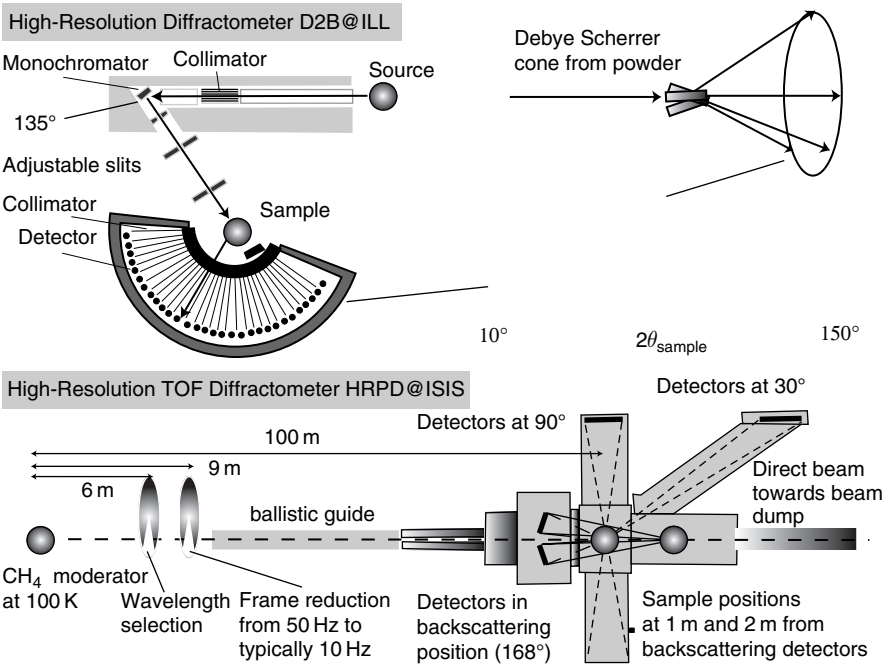

Fig. 3.15 Schematics of powder diffractometers. The fixed wavelength or angular-dispersive diffractometer uses the Bragg reflection from a crystal to define a monochromatic incoming beam. The better defined the divergence before and after the monochromator and the larger the scattering angle $2\theta_{\text{mono}}$ (135° in the case of D2B@ILL), the higher the wavelength resolution $\Delta\lambda/\lambda$ (see Eq. (3.64)). The overall Q-resolution depends on the scattering angle $2\theta_{\text{sample}}$ at the sample and on the collimation between sample and detector. It varies strongly with $2\theta_{\text{sample}}$ (see Eq. 3.64). The scattered intensity is recorded over the full angular range using a large position-sensitive detector (PSD). As for three-axis spectrometers, configurations with alternating sense of scattering at monochromator and sample offer better $\vec{Q}$-resolution. Powder samples lead due to the random orientation of the crystallites to scattering concentrated in cones around the incoming wavevector. Each cone properly integrated over the PSD gives a powder line in the diffraction pattern $I(2\theta_{\text{sample}})$. In the case of a time-of-flight or wavelength-dispersive spectrometer, the incoming wavelength varies as a function of time. One, therefore, obtains diffraction patterns as a function of the d-spacing in any pixel of the large area PSDs. This is particularly useful when heavy sample environment like pressure cells limit the available scattering angles. The longer the flight path the higher the wavelength resolution (see Eq. (3.70)). Highest overall resolution is obtained in backscattering at the sample (Eq. (3.37)). Efficient neutron transport is achieved by ballistic neutron guides.

(hkl)-points. The efficiency of the measurement can be enhanced by using two-dimensional position-sensitive detectors (PSD). The $\vec{Q}$-resolution of a single crystal spectrometer is sufficient, if it allows the clear separation of the Bragg peaks of interest. The density of Bragg peaks increases with the size of the unit cell. For larger unit cells it is preferable to work with longer wavelengths. The resolution in real space is determined by the shortest d_{hkl}-spacings that can be measured. It thus improves with shortening the wave-length. Good Q and d resolution are, therefore, conflicting requirements.

In an ideal powder sample, small crystallites are oriented randomly (see Fig. 3.15). The scattering from a particular set of lattice planes corresponds to the scattering obtained by turning a single crystal oriented in Bragg scattering geometry about the direction of the incoming beam, that is, instead of Bragg-peaks we obtain *Debye-Scherrer cones*, whose non-uniform intensity thereby indicates preferred orientation of diffracting grains. Intensity from the cones can be determined simultaneously using large-area detector arrays.

The deviation from ideal randomization is called *texture* (that is, preferred orientation) and a particularly interesting subject of investigation for earth sciences (see Fig. 3.16). It is the goal of the texture investigation to determine the distribution of crystal orientations

$$f(\mathbf{G}(\psi_1, \phi, \psi_2)), \qquad \mathbf{G} = [G_{i,j}], \tag{3.62}$$

that is, the probability of finding a crystal in an orientation described by the rotation matrix $\mathbf{G}$ with respect to a fixed reference frame. (ψ_1, ϕ, ψ_2) denote the three Euler angles. Neutron diffraction probes the orientation of planes. For a given (hkl) a texture measurement is thus insensitive to the part of $\mathbf{G}$ that maps the plain (hkl) onto itself. The full three-dimensional orientational distribution of the crystal $f(\mathbf{G}(\psi_\mathbf{1}, \phi, \psi_\mathbf{2}))$ has to be constructed mathematically from the two-dimensional projections,

$$P_{hkl}(\alpha, \beta) = \frac{1}{2\pi} \int_{\psi} f(\mathbf{G}) \mathrm{d}\psi, \tag{3.63}$$

of a set of lattice plains $[hkl]$. ψ denotes the angle of rotation about an axis perpendicular to the planes. α and β denote the tilting and rocking of the plane (see Fig. 3.16). While a single crystal is fully oriented when two planes are identified [26], the inversion for arbitrary P_{hkl} has, generally, no unique solution. The measured reduced distributions are normally presented as projections onto a flat surface giving so-called *pole figures* [45].

The resolution of a fixed wavelength diffractometer depends according to Eq. (3.37) on the collimation of the beams and the scattering angles at the monochromator and the sample [46]. The full width at half maximum of the powder peaks can be well described by the equation

$$\Delta^2_{\mathrm{FWHM}} = U \tan^2 \theta_{\mathrm{sample}} + V \tan \theta_{\mathrm{sample}} + W, \tag{3.64}$$

with the prefactors U, W and V, being complex functions of the beam divergences and of the monochromator angle θ_{mono}. The minimum of that function occurs for

$$\tan \theta_{\mathrm{sample}} = -\frac{V}{2U} \approx \tan \theta_{\mathrm{mono}}, \tag{3.65}$$

[26] In that case $P_{hkl}(\alpha, \beta) = \delta(\alpha - \alpha_0)\delta(\beta - \beta_0)$.

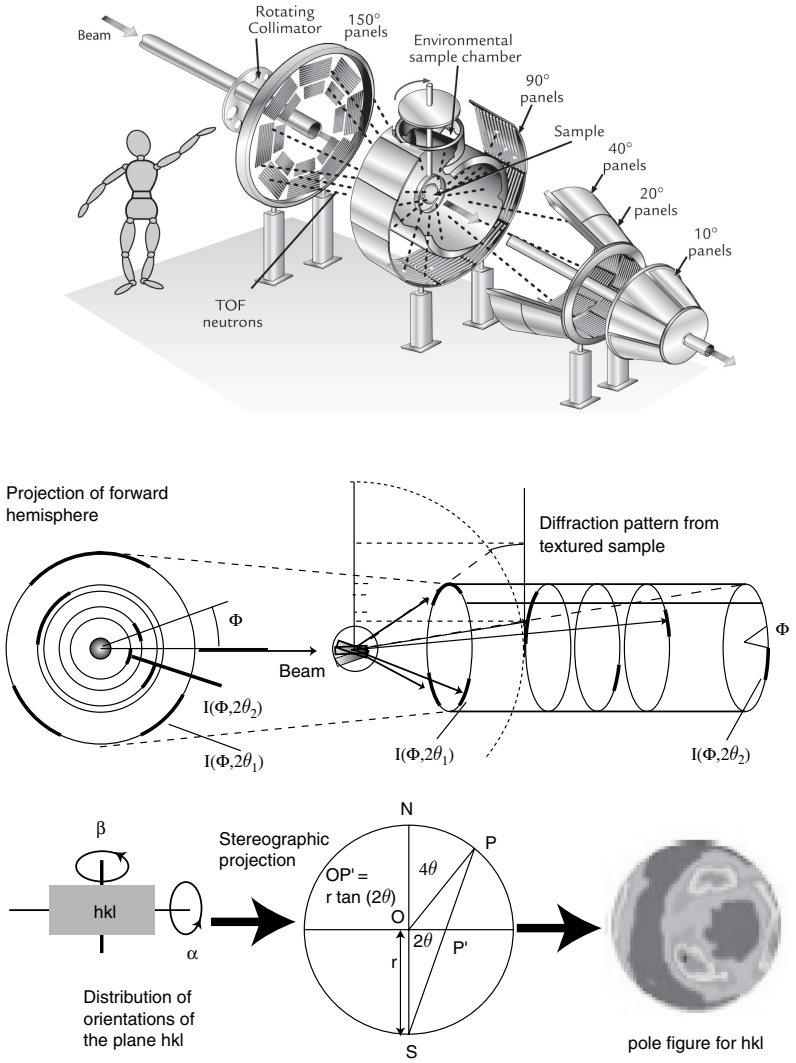

Fig. 3.16 Texture. Schematic view of the time-of-flight diffractometer HIPPO at Los Alamos Neutron Science Center (LANSCE). The detector tubes are arranged in panels on rings of constant diffraction angle. The intensity can be gathered with equal quality for all Φ simultaneously. The schematic drawing shows the scattering arising from a distribution of crystal orientations. When the crystallites in the sample are not randomly oriented, the diffraction pattern deviates from isotropic Debye–Scherrer rings. The anisotropy can, for example, be created by shear or uniaxial pressure during the material's formation. To retrieve the orientational information we have to determine the intensity I as a function of the rotation angle Φ about the incoming beam. For graphical display $I(\Phi)$ can be projected onto a sphere and from the sphere onto the sphere's equatorial plane. The mechanism used here is the Lambert projection, which has the nice property of conserving areas. By using different sample orientations it is possible to determine the distribution of a given lattice plain (h, k, l). This distribution can be displayed by projecting it from a sphere onto a plain. This produces so-called pole figures. If the stereographic projection is used, then angles are conserved

that is, when the scattering angle at the sample is close to the monochromator angle. It is possible with high-resolution diffractometers like D2B at the ILL (see Fig. 3.15) to attain resolutions of 0.1° equivalent to $\Delta d/d \approx 5 \cdot 10^{-4}$. This is in the order of the limit set by the line broadening due to the *primary extinction* in the crystallites. Opening up the beam divergence and going to larger d-spacings for the monochromator (that is, lower take-off angles for a given wavelength) increases flux at the expense of resolution. This can be important in the case of kinetic studies.

Using adapted collimation systems it is possible to illuminate only small, so-called *gauge volumes*, of the sample.[27] This allows to scan large samples for variations in scattering patterns. The variation of the lattice spacing, for example, monitors the strain in a material. In the same way one can follow the spacial variations of crystallographic phases or texture. The method equally works for small angle scattering (see Section (3.4.6)) and can be used together with radiography and tomography to *image* samples.

3.4.5 Time-of-Flight Diffractometers

An indirect time-of-flight spectrometer can be turned into a diffractometer in the same way as a three-axis spectrometer, that is, by taking out the analyzers [47] (see Figure 3.15). This allows determining the energy integrated differential cross section $\mathrm{d}\sigma/\mathrm{d}\Omega$ by recording the intensity as a function of the arrival time in the detector. It is instructive to calculate the observed spectrum for simple Bragg scattering. To this end we design a simple time-of-flight diffractometer consisting of an initial flight path L_{ps} from the pulse creation device to the sample plus a single detector at a scattering angle 2θ at a distance L_{sd}. Neutrons will be deflected into the detector, if the wavelength (see Eq. (3.43))

$$\lambda = \frac{h}{mL}t \tag{3.66}$$

satisfies the Bragg equation, that is, if

$$d = \frac{h}{2mL\sin\theta}t_{hkl}, \tag{3.67}$$

with $L = L_{\mathrm{ps}} + L_{\mathrm{sd}}$ denoting the total flight path. If we turn the crystal in the beam or if we use a powder sample, then we expect for every lattice plan (hkl) a peak in the detector at time t_{hkl}, which is linked to the respective lattice spacing d_{hkl} via the simple relation

[27] The shape of the gauge volume depends on the scattering angle. It is a rectangular solid with a square base in the case of $2\theta = 90^\circ$.

$$d_{hkl}[\text{Å}] = \frac{1.978 \cdot 10^{-3}}{\sin\theta} \frac{1}{\text{L[m]}} t_{hkl}[\mu\text{s}]. \tag{3.68}$$

Inverting the above equation leads to the spectrum observed under a particular detector angle as a function of time:

$$t_{hkl}[\mu\text{s}] = 5.0556 \cdot 10^2 \cdot \text{L[m]} \cdot d_{hkl}[\text{Å}] \cdot \sin\theta. \tag{3.69}$$

So in the backscattering mode ($\theta = 90^\circ$) and with a flight path of 100 m, a 1 Å difference in lattice spacing will lead to a peak separation of about 50 ms. This assumes that the necessary wavelengths are present in the spectrum. According to Eq. (3.67) this implies a minimum bandwidth of 0.5 Å. During the 50 ms measuring time it is clear that no neutrons from another source pulse can be allowed to arrive in the detector. The 0.5 Å wavelength band thus translates into a maximum source frequency of 20 Hz.

Equation (3.67) depends on the three variables t, L, and θ. If we assume that they vary independently, then the relative resolution is given as

$$\frac{\Delta d}{d} = \sqrt{\left(\frac{\Delta t}{t}\right)^2 + \left(\frac{\Delta L}{L}\right)^2 + \Delta\theta^2 \cot^2\theta}. \tag{3.70}$$

In a time-of-flight diffraction pattern, contributions varying with wavelength have to be corrected for. The most prominent is the effect on the intensity of a Bragg reflection, which goes as

$$I_{hkl} \propto I(\lambda)|F_{hkl}|^2 \lambda^4 \cot\theta \Delta\theta. \tag{3.71}$$

Absorption is normally a linear function of λ. Extinction and, in particular, inelastic corrections are more complicated.

Like in the case of the fixed wavelength diffractometers, data on time-of-flight diffractometers are collected over large solid angles using position-sensitive detectors. The resolution is best in backscattering geometry. Lateral detector banks $2\theta = 90^\circ$ are particularly useful in the case of heavy sample environment, like pressure cells.

3.4.6 SANS Instruments

There is a continuously increasing interest in the study of objects from the nanometer to micrometer range. This requires a particular instrumentation capable of measuring $S(\vec{Q})$ with good precision for small $\vec{Q}$ values. The need for small Q may be easily seen in the case of Bragg scattering. Using the relation

$$Q = \frac{4\pi}{\lambda} \sin\theta, \tag{3.72}$$

we may rewrite the Bragg equation (Eq. 3.34) in the form

$$Q = \frac{2\pi}{d}. \tag{3.73}$$

This demonstrates that smaller Q vectors probe larger lattice plane distances d. This statement holds more generally as the scattering function $S(Q, \hbar\omega)$ is determined by scattering density correlations on the scale $2\pi/d$. In order to investigate objects extending from about 1 nm to 100 nm, we thus need rather small Q-values in the range of $10^{-3} to 10^{-1}$ Å^{-1}. For a given wavelength λ this can only be achieved by going to very small scattering angles, hence the name of *Small Angle Neutron Scattering* or SANS.[28] The classical small-angle instrument uses a *pin-hole geometry*, that is, it defines the beam divergence through apertures placed at a well-chosen distance from each other.[29]

The $\vec{Q}$-resolution of a small-angle instrument is given by the uncertainties in wavelength λ and scattering angle 2θ. The wavelength distribution of the incoming beam is determined either by the velocity selector (see Section 3.3.7) or in the case of a pulsed source by the pulse width Δt and flight time t of the beam [48]. The uncertainty in the scattering angle is due to the finite character of the beam divergence, sample size, and detector resolution. Using the notation introduced in Fig 3.17 we get

$$\frac{\Delta\theta}{\theta} = \frac{\sqrt{\arctan^2\left(\frac{d_1+d_2}{2(L_1+L_2)}\right) + \arctan^2\left(\frac{d_2+\Delta D}{4L_2}\right)^2}}{\arctan\frac{D}{2L_2}}. \tag{3.74}$$

For small angles and a primary flight path L_1 not too different from the secondary flight path L_2, this can be simplified to

$$\frac{\Delta\theta}{\theta} \approx \frac{(d_1+d_2)^2 + (d_2+\Delta D)^2}{4D}. \tag{3.75}$$

Typically, apertures, sample size, and detector pixels are in the centimeter range. This leads to uncertainties in $\Delta\theta/\theta$ that vary with $1/D$ and range from close to 50% near a 5×5 cm^2 beam stop to 5% at the periphery of a 1×1 m^2 detector. It may seem surprising that $\Delta\theta/\theta$ does not, to a first approximation, depend on L. The length L

[28] If there were means of moderating the neutron spectrum efficiently down to even lower temperatures, that is, of achieving high neutron flux at wavelengths ranging from 10 to 1000 Å, large objects could in principle be investigated at wider angles. In practice one would, however, reach limits due to the high absorption and finally weak penetration (see Section 3.4.7) of long-wavelength neutrons.

[29] We will assume in the following circular apertures. In practice one often uses the guide opening with a rectangular aperture in front of the sample. This introduces an asymmetry in the divergence contribution to the resolution.

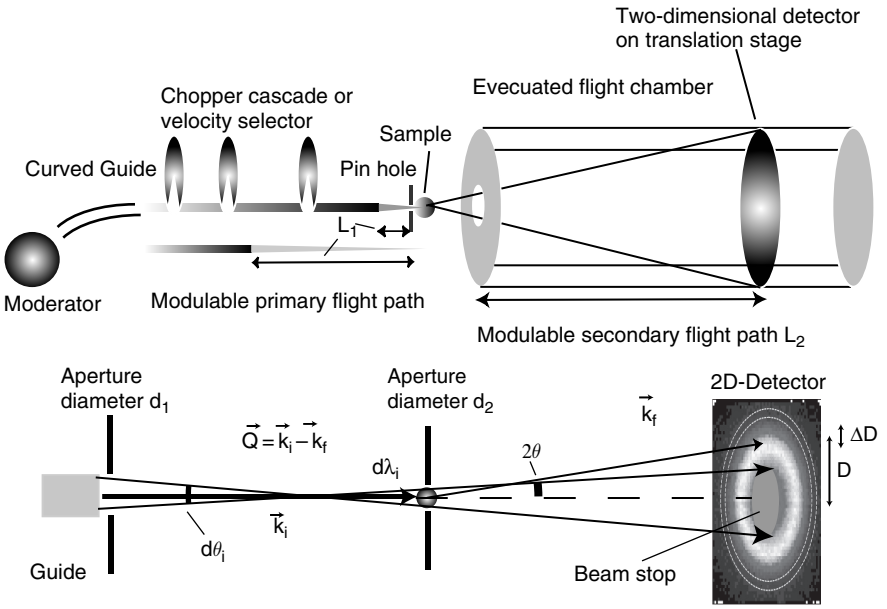

Fig. 3.17 Schematics of a small-angle scattering instrument. The wavelength selection is either performed by a velocity selector or by a chopper cascade, depending on whether one prefers to work in continuous or time-of-flight mode. In the latter case $\vec{Q}(\theta;t)$ is a function of time, while in the former case it is constant. The incoming beam is defined by a set of apertures d_1 and d_2 placed at a collimation distance L_1 typically between 10 and 30 m. The size of the apertures defines the divergence that can be transmitted through the system without scattering at the sample. This direct beam creates a dark area on the detector covered by a beam stop. If the instrument is well designed, the intensity due to parasitic scattering should drop off by several orders of magnitude within a few millimeters from the beam stop. The beam is transported up to the first aperture by a guide system. The guide system itself is highly adjustable allowing an easy variation of L_1. It assures an optimal filling of the beam defined by the apertures. If for example the maximum divergence $\Delta\theta_i < 0.5°$, then for $\lambda > 5$ Å a normal Ni coating of the guide is sufficient. The second aperture is placed close to the sample. The detector is placed in an evacuated flight tube. It has a typical size between $50 \times 50\,\mathrm{cm}^2$ and 1×1 m. It is mounted on a translation stage that allows varying the distance L_2 to adapt it to L_1. Some SANS machines offer off-center positioning of the beam to cover higher Q-values

has, however, a very strong influence on the absolute Q-resolution. This is due to the fact that L defines—for a given wavelength λ—at what distance D the signal corresponding to a particular Q will be observed in the detector.

$\Delta\lambda/\lambda$ is primarily determined by the velocity selector or time-of-flight system and thus basically independent of $\Delta\theta/\theta$. We thus can add both contributions quadratically to get:

$$\frac{\Delta Q}{Q} = \sqrt{\left(\frac{\Delta\lambda}{\lambda}\right)^2 + \left(\frac{\Delta\theta}{\theta}\right)^2}. \tag{3.76}$$

Given the relaxed resolution in angle it is possible to work with rather large wavelength bands in the range from 10% to 15%. The instrument is usually arranged so that $\Delta\lambda/\lambda = \Delta\theta/\theta$ about half way out from the beam centre to the edge of the detector.

The rather coarse wavelength resolution required for SANS measurements is a problem for pulsed sources. As $\Delta\lambda/\lambda = \Delta t/t \approx \tau_p h/mL\lambda$ and as the flight path length L is fixed by the angle required to reach Q, the wavelength resolution is generally too good even for long pulse lengths τ_p. This implies an unavoidable loss of intensity. Time-of-flight SANS instruments at continuous sources have the advantage that they can use arbitrarily broad pulses created by choppers.

The relative resolution of the SANS diffractometer lying in the 10% range it is essential to tune the Q-value correctly to the size of the object under investigation. For 1000 Å objects, 15 m sample-detector distance and 5 Å neutrons ($10^{-3} < Q < 10^{-1}$) may be a good choice, while for 10,000 Å objects, 30 m and 20 Å ($10^{-4} < Q < 10^{-2}$) are certainly recommended, despite the fact that the flux from the cold source will be drastically reduced in this range (see Section 3.2.2).

3.4.7 Reflectometers

All instruments discussed so far study samples in the bulk. We have seen in Section 3.3.4 that the neutron has an index of refraction. This property can be converted into a powerful tool for studying surfaces and interfaces (see Fig. 3.18). Specular reflection gives information on the profile of the scattering-length density $\sum_i N_i b_i$ perpendicular to the surface. The information is contained in the drop of reflectivity for reflection angles larger than the critical angle. As the drop is drastic (see Fig. 3.6), the instrument performance relies on high sensitivity. Good reflectometers can determine reflectivity changes from 1 to 10^{-8}. As can be seen in Fig. 3.18 the interference fringes in the reflectivity arising from layers of different scattering density are to a good approximation separated by $2\pi/d$, with d denoting the thickness of the layers. As the Q-range is equally set by $2\pi/d$, the relative resolution requirement $\Delta Q/Q$ is similar to the SANS case, that is, it is in the order of a few percent%. Therefore, higher resolution and lower Q are needed to determine the scattering length density profile on a longer length scale, while thin films can be studied with rather modest resolution at larger Q. In the way particle size dispersion smears out the SANS pattern, interface roughness smears out the specular reflectivity curve.

When neutrons are scattered from laterally homogeneous stratified media, only specular reflection is observed. Sample inhomogeneities, such as interfacial roughness or voids, give rise to off-specular scattering. The easiest way to describe this scattering theoretically is based on the distorted-wave Born approximation (DWBA) [49, 50], which uses the neutron wavefunctions that describe reflection from a smooth surface as the basis functions for perturbation theory.[30]

[30] For a nice example see [51].

If the beam impinges on the surface below the critical angle, then the corresponding evanescent wave field will penetrate the surface layer. Within this layer it can be scattered laterally (for the geometry see Fig. 3.18) leading in the case of large objects to a small-angle signal (*Grazing Incidence Small Angle Scattering* or GISANS). If the layer is laterally ordered, the evanescent wave may be diffracted (*Grazing Incidence Diffraction*).

As the angles of reflection are always small (see Eq. (3.33)) the resolution of a reflectometer is given to a good approximation by the expression Eq. (3.76) used for small-angle scattering. Reflectometers need a beam with very small divergence (in the order of 1–10 min of arc) in the plane of reflection. This is achieved with the help of slits. The Q value can be varied either by using a monochromatic beam

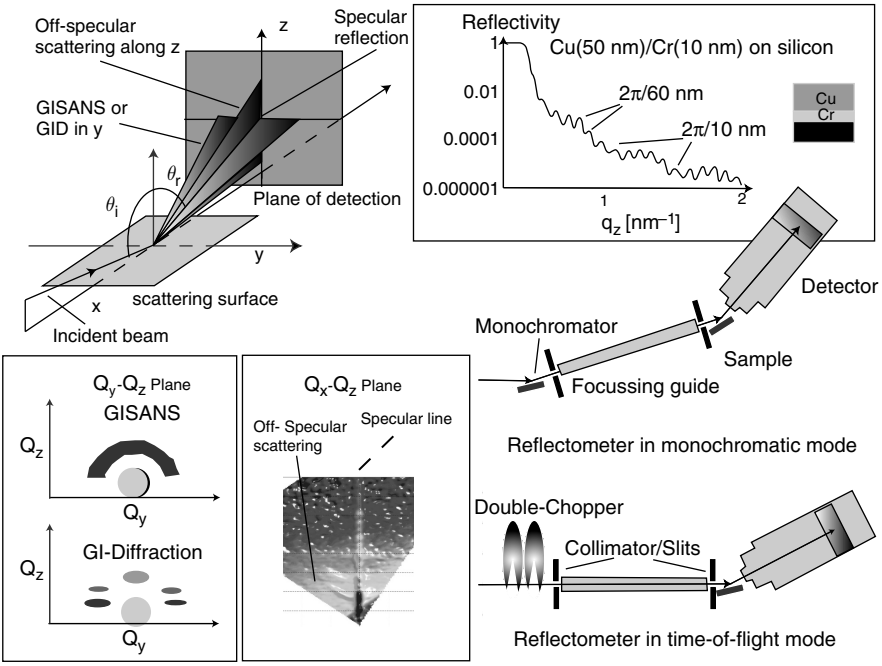

Fig. 3.18 Schematics of a reflectometer. The incident beam is hitting the surface or interface close to the critical angle. Under specular reflection $\theta_i = \theta_r$ we can follow the scattering length density as a function of depth below the surface. The reflectivity drops off quickly as soon as we are above the critical q_z. With neutron reflectometry it is typically possible to cover 6–8 orders of magnitude in reflectivity. The shown reflectivity profile of a layered thin film gives an idea of the signal. The distance between the fringes is directly related to the film thickness. High resolution is required for thick films. Off-specular scattering probes correlations in the x-direction. If the beam is impinging below the critical angle, then the corresponding wave-field explores a surface layer with a thickness corresponding to the penetration length. Within this layer it can be scattered laterally. If there is order like in a crystal, we will get Bragg-scattering called grazing incidence diffraction. In the case of larger randomly arranged objects we end up with grazing incidence small-angle scattering (GISANS). Reflectometers like the one shown here (D17 at the ILL) work either in a monochromatic or in a time-of-flight mode

and changing the angle of incidence or by using an energy-dispersive beam and the time-of-flight method. Reflectometers offer in this way a range from about 0.005 to 1.5 $Å^{-1}$. They thus can probe length scales perpendicular to the surface from 4 Å to about 1000 Å.

In the case of grazing incidence the volume probed is defined by the penetration of the *evanescent wave*

$$\psi_e \propto \mathrm{e}^{-\frac{1}{2}\sqrt{q_c^2-q^2}\cdot z}, \qquad q < q_c, \tag{3.77}$$

which can be taken as

$$d_{\text{penetration}} = \frac{2}{\sqrt{q_c^2 - q^2}}. \tag{3.78}$$

For example, on a silicon surface this penetration is about 100 Å at $q = 0$ and diverges at $q = q_c$. The divergence has the surprising consequence that the q_c is not altered when a thin film—let us say 100 Å of Ni on Si—is put on a substrate.

For off-specular scattering Q_x is the relevant parameter. As $Q_x = Q_z \cdot \sin\epsilon$, with ϵ denoting the deviation of the reflected beam from the specular line the accessible length scales are considerably longer ranging from about 0.1 to 100 μm.

On a continuous source the monochromatic option allows to select the wavelength corresponding to the maximum in the spectrum of the source, while in the time-of-flight mode a large part of the spectrum has to be utilized. The time-of-flight option has the advantage that the full Q-range can be covered simultaneously, which is very important for kinetic studies. It equally allows for an easy variation of the wavelength resolution. In addition, the reflection angles are invariant. In the monochromatic mode the reflection angle has to be varied, implying a readjustment of the sample position along the $\hat{z}$-direction. Most neutron guides are higher than wide. It is, therefore, easier to build a reflectometer like a classical diffractometer with a horizontal scattering plane focusing the beam in the vertical direction, where the divergence has little influence on the resolution, onto the sample (in the case of GISANS or GI-Diffraction this may no longer be the case and a tighter collimation has to be introduced). This implies a vertical sample position, which is not suited for studying liquid surfaces. Reflectometers for horizontal sample positions use dedicated guides that create a beam with a large horizontal divergence at the sample position.

3.4.8 Spin-Echo Spectrometers

All the spectrometer concepts that we have discussed so far incorporate mechanisms for adjusting the energy resolution. As with the standard devices the phase space volumes can be reshaped but not compressed (Liouville theorem), this implies trimming the wavelength bands of both the incoming and the scattered beam. Even if this is done in the most economic way, it leads to a loss in intensity that goes

at least with the inverse square of the energy resolution. One of the main keys to successful high-resolution neutron spectroscopy in the Liouville limited domain is the decoupling of energy and Q-resolution. This permits, as we have demonstrated for the backscattering spectrometer (see Section 3.4.2), sub-μeV resolution with acceptable count rates for experiments that tolerate a rather poor Q-resolution.

In soft matter or liquids we are very often interested in studying very slow processes. An exponential relaxation of the form

$$I(t) = I_0 \exp(-t/\tau) \tag{3.79}$$

leads to a Lorentzian form of the corresponding scattering function

$$S(\hbar\omega) = I_0 \int_0^\infty e^{-i\omega t} e^{-\frac{t}{\tau}} \mathrm{d}t = \frac{I_0\tau}{1+(\omega\tau)^2} = \frac{I_0\tau}{1+(E\tau/\hbar)^2}. \tag{3.80}$$

The half-width half-maximum of this function is given by

$$\Delta E_{\mathrm{HWHM}} = \frac{\tau}{\hbar}. \tag{3.81}$$

This leads to the relation,

$$\tau[\mathrm{ns}] = 0.66/\Delta E_{\mathrm{HWHM}}[\mu\mathrm{eV}], \tag{3.82}$$

between the measurable relaxation time τ of the system and the required energy resolution ΔE of the spectrometer. Therefore, in backscattering we are sensitive to time scales of the order of 1 ns.

To study even longer times requires the use of spin-echo spectrometers. This technique makes a very efficient use of neutrons. It encodes the change of the velocity distribution function $\Delta p(v)$ occurring at the sample in the polarization $\vec{P}$ of the beam. The encoding of the change $\Delta p(v)$ is to a first approximation independent of the velocity distribution function $p(v)$ itself. This method thus allows for the use of a rather broad wavelength band with correspondingly high beam intensities.

We will in the following develop the main ideas of classical spin-echo spectroscopy.[31] Deducing the formula relating the measured signal to its interpretation as the time Fourier transform of the scattering function will require a sufficiently detailed discussion of polarized beam manipulation. This explains the length and the more mathematical character of this section. We will, however, try to stay close to the experimental observables.

[31] Spin-echo spectroscopy was invented by Feri Mezei in 1972 [52]. We adopt in our presentation an approach similar to that used in the introduction to spin-echo spectroscopy by Mezei [53, 54], Cywinski [55], and Lechner–Longeville [41].

We start by giving a short overview of the basic formalism of *beam polarization*. The neutron is a fermion that carries a spin $s = 1/2$. This translates into the fact that the quantum mechanical state of the neutron evolves within a two-dimensional space.[32] The link of the quantum states to the three components of the spin vector $\vec{\mathbf{S}}$, which is a quantum mechanical observable in real space, is provided through the Pauli spin operators

$$\sigma_x = \begin{bmatrix} 0 & 1 \\ 1 & 0 \end{bmatrix}, \ \sigma_y = \begin{bmatrix} 0 & -i \\ i & 0 \end{bmatrix}, \ \sigma_z = \begin{bmatrix} 1 & 0 \\ 0 & -1 \end{bmatrix}, \tag{3.83}$$

with

$$\vec{\mathbf{S}} = \frac{\hbar}{2}\vec{\sigma}. \tag{3.84}$$

Any quantum state of the neutron can be written as a coherent superposition

$$|\chi >= a_+|+ > +a_-|- >, \ \ |a_+|^2 + |a_-|^2 = 1 \tag{3.85}$$

of two orthogonal basis vectors $|+ >$ and $|- >$, which we take for matters of practicality as the eigenvectors of the Pauli matrix σ_z with eigenvalues of $+1$ and -1. The coefficients $a_\pm$ are to be identified with the wave functions $\psi_\pm(\vec{r}, t)$ of the particle. They contain, for example, the energetic Zeeman splitting of the two spin components in an applied magnetic field (see below). To render notation more fluent

---

[32] This is a direct consequence of special relativity. The Dirac equation

$$\mathbf{H}\psi = (c \cdot \vec{\alpha} \cdot \vec{\mathbf{p}} + \beta mc^2)\psi \tag{3.86}$$

is relativistically invariant if, and only if,

$$\mathbf{H}^2\psi = c^2(\vec{\mathbf{p}} \cdot \vec{\mathbf{p}} + c^2m^2)\psi. \tag{3.87}$$

$\vec{\mathbf{p}} = -i\hbar\vec{\nabla}$ is the momentum operator. This implies that the coefficients α_i and β satisfy the anti-commutation relations

$$\alpha_i\alpha_j + \alpha_j\alpha_i = 2\delta_{ij}\mathbf{1}, \tag{3.88}$$

$$\alpha_i\beta + \beta\alpha_i = 0, \tag{3.89}$$

$$\beta^2 = \mathbf{1}, \tag{3.90}$$

with $\mathbf{1}$ denoting the unit matrix and $i, j = x, y, z$. It can be shown that at least four dimensions are required to represent such an algebra. A possible choice for the (4×4) matrices is given by

$$\alpha_i = \begin{bmatrix} 0 & \sigma_i \\ \sigma_i & 0 \end{bmatrix}, \ \beta = \begin{bmatrix} \mathbf{1} & 0 \\ 0 & -\mathbf{1} \end{bmatrix}, \tag{3.91}$$

with σ_i denoting the (2×2) Pauli matrices. In vacuum the only symmetry breaking direction is give by the momentum $\vec{p}$ of the neutron. Without loss of generality the $\hat{z}$-direction can be choosen to coincide with $\hat{p}$. The four components of the Dirac wave function then correspond, respectively, to particle and anti-particle of positive (spin aligned parallel to $\hat{p}$) and negative (spin aligned anti-parallel to $\hat{p}$) helicity.

the space-time dependence of the wave function will not be explicitly mentioned in those cases where we are dealing with quantum mechanical problems consisting in manipulating the spin variables of free neutrons.

The neutron spin manifests itself experimentally via its *coupling to magnetic fields*. The interaction potential of the neutron with matter[33] comprises, therefore, a magnetic contribution

$$V_{\mathrm{m}} = -\vec{\mu}_n \cdot \vec{B}(\vec{r}) \tag{3.92}$$

given by the scalar product of the magnetic field $\vec{B}$ with the magnetic moment operator of the neutron

$$\vec{\mu}_n = (\gamma_n \mu_N)\,\vec{\sigma} = (\gamma_n \mu_N)\frac{2}{\hbar}\,\vec{\mathbf{S}} = \gamma_L\,\vec{\mathbf{S}}. \tag{3.93}$$

$\gamma_n = -1.91304275(45)$ denotes the neutron's magnetic moment in units of the nuclear magneton μ_N and $\gamma_L = -1.832 \times 10^8$ rad·s^{-1}·T^{-1} stands for the gyromagnetic ratio of the neutron.

Inside magnetic materials the magnetic field felt by the neutron includes, in addition to the applied external field, the magnetization $\vec{M}$ of the sample[34]

$$\vec{B} = \mu_0(\vec{H}_{\mathrm{applied}} + \vec{M}). \tag{3.94}$$

We will now discuss how the interaction with magnetic fields allows the manipulation of a polarized neutron beam [56]. We start by giving a precise meaning to the term polarization. When leaving the moderator, the neutrons can be considered a paramagnetic non-interacting gas of fermions. Polarized neutron beams are characterized by a finite magnetization given by the expression

$$\begin{aligned} < \vec{\mathbf{M}}_n(\vec{r}, t) > &= \gamma_n \mu_N < \vec{\sigma}(\vec{r}, t) > \\ &= \gamma_n \mu_N \int \mathrm{d}^3k \sum_{\chi} p(\vec{k}, \chi) < \vec{k}, \chi | \vec{\sigma}(\vec{r}, t) | \vec{k}, \chi > \end{aligned} \tag{3.95}$$

with $p(\vec{k}, \chi)$ describing the distribution of the beam in terms of k-vector and spin state χ at any point and time. The expectation value

$$\vec{P}(\vec{r}, t) = (1/V) \int \mathrm{d}^3k \sum_{\chi} p(\vec{k}, \chi) < \vec{k}, \chi | \vec{\sigma}(\vec{r}, t) | \vec{k}, \chi > \tag{3.96}$$

[33] This contribution adds to the nuclear interaction described by the Fermi pseudo-potential introduced in Eq. 3.26

[34] As the magnetization of the neutron gas is very small, we are not obliged to make a distinction in between the magnetic field $\vec{H}$ and the magnetic flux density $\vec{B}$ outside magnetic materials.

is called the beam polarization, with $V = \int \mathrm{d}^3k \sum_\chi p(\vec{k}, \chi)$ denoting the phase space volume.

If we restrict ourselves to one particular quantum state $|\chi >$, then we can relate the orientation of $\vec{P}_\chi$ to the coefficients of the quantum state introduced in Eq. (3.85) by using the explicit form of the Pauli spin-matrices of Eq. (3.83):

$$a_+ = e^{-i\frac{\phi}{2}} \cos\frac{\theta}{2}, \tag{3.97}$$

$$a_- = e^{i\frac{\phi}{2}} \sin\frac{\theta}{2}, \tag{3.98}$$

with the spherical coordinates $0 \leq \theta \leq \pi$ and $0 \leq \phi < 2\pi$ defining the orientation of $\vec{P}_\chi$ with respect to the magnetic field (see Fig. 3.19). For example, a neutron polarized along the direction $\hat{x}$ perpendicular to the magnetic field is described by the quantum state

$$|+>_x = \frac{1}{\sqrt{2}} \left(|+>_z + |->_z\right), \tag{3.99}$$

as can be easily verified by calculating the expectation value of $\vec{P}$ according to Eq. (3.96).

A polarized beam can be produced from the paramagnetic neutron gas exploiting magnetic interaction. In neutron spin-echo spectroscopy, the standard technique of polarizing a beam consists in reflection from a magnetically birefringence medium. The index of refraction, which we had introduced in the section on neutron mirrors and guides (see Eq. (3.28)), reads in the magnetic case as

$$n_\pm = 1 - \frac{\lambda^2}{2\pi} \sum_i N_i b_i \pm \frac{m\lambda^2}{h^2} \vec{\mu}_n \cdot \vec{B}, \tag{3.100}$$

where the indices $\pm$ refer to the two quantum eigenstates of the neutron in the applied field. This difference in n allows polarizing the beam in reflection (only one spin state is reflected) or transmission (only one spin state is transmitted) (see Fig 3.19). Other possibilities of beam polarization are spin discriminating Bragg reflection (Bragg scattering is active only for one spin component), spin-dependent absorption in a polarized ^{3}He-filter (only one spin state is absorbed) or separation of spin components in a strong magnetic field gradient like in a Stern-Gerlach type set-up or in strong hexapolar magnets. The later method is, for example, used for ultra cold neutrons or helium.

A polarized neutron beam can be manipulated using magnetic fields. The evolution of the magnetization of the neutron beam if subjected to a magnetic field $\vec{B}$ is described by the equation

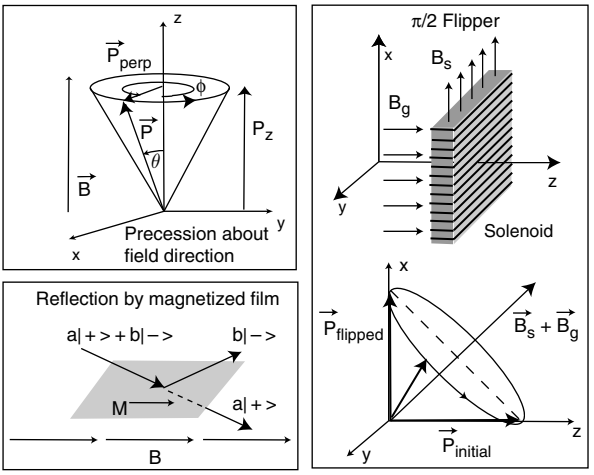

Fig. 3.19 Polarized neutron beams. The neutron interacts with magnetic fields via its magnetic moment. A polarized neutron beam is characterized by a finite magnetization corresponding to an alignment of the magnetic moments. Polarized beams can be created, for example, via reflection from a magnetized multilayer (super-mirror). As the reflectivity depends on the alignment of the neutron's magnetic moment with respect to the magnetization of the film, it is possible to design devices that allow selecting one of the two spin components of the neutron either in transmission or in reflection. The main problem of such polarizers is the limited angular acceptance. Polarized neutron beams are transported via guide fields. The component of the beam polarization $\vec{P}_\perp$ that is perpendicular to the field direction precesses around the field with the Larmor frequency, while the component parallel to the field is stationary. For a slow change of the guide field, the parallel component of the polarization will adiabatically follow the field. The orientation of the polarization with respect to the field, therefore, is preserved. If the field changes abruptly, the polarization $\vec{P}$ has no time to adapt and will start to precess about the new direction. This fact is exploited to reorient the polarization of the beam with respect to the field. In the case of a $\pi/2$-flipper a solenoid creates a field $\vec{B}_s$ that together with the guide field $\vec{B}_g$ leads to a total field $\vec{B}_t = \vec{B}_s + \vec{B}_g$ at 45° with respect to the initial beam polarization (along $\vec{B}_g$). The neutron beam spends just enough time in the field region of the solenoid to perform a 180° rotation about $\vec{B}_t$. When leaving the solenoid non-adiabatically, the polarization is now perpendicular to the guide field, that is, it has performed a 90° or $\pi/2$ turn. In the spin-echo technique this flip corresponds to $t = 0$ as it starts the precession motion within the spin-echo coils (see Fig. 3.20). A π-flipper (not shown) needs a horizontal field close to zero and a vertical field strong enough to turn the polarization by 180° during the flight-time of the neutron within the flipper coil

$$\frac{\mathrm{d} < \vec{\mathbf{M}} >}{\mathrm{d}t} = -\gamma_L(< \vec{M} > \times \vec{B}), \tag{3.101}$$

which reads in terms of the polarization

$$\frac{\mathrm{d}\vec{P}}{\mathrm{d}t} = -\gamma_L(\vec{P} \times \vec{B}). \tag{3.102}$$

For $\vec{B}$ directed along $\hat{z}$ we find the solutions

$$\begin{aligned} P_x(t) &= \cos(\omega_L t)P_x(0) - \sin(\omega_L t)P_y(0), \\ P_y(t) &= \sin(\omega_L t)P_x(0) - \cos(\omega_L t)P_y(0), \\ P_z(t) &= P_z(0). \end{aligned} \tag{3.103}$$

The components of $\vec{P}$ perpendicular to the field thus precess about $\hat{B}$ with the *Larmor frequency* $\omega_L = -\gamma_L B$ (see Fig 3.19).

Once the neutrons have left the moderator they are a priori in a collision-less regime. Despite this fact, a *guide field* is required to maintain the magnetization of the neutron beam as even small magnetic perturbations would quickly lead to depolarization.[35] The coordinate system is chosen such that the direction of the guide field coincides with the $\hat{z}$-axis.

If the direction of the guide field is changed slowly, then the neutrons will follow this change *adiabatically* meaning that the polarization of the beam will always precess about the local magnetic field direction with the projection of the polarization upon $\vec{B}$ remaining unchanged. If, to the contrary, the change of field is abrupt, then the neutron cannot adapt to it and will carry its original polarization into the new field region, where it will start precessing about the new field direction according to Eq. (3.103). *Non-adiabatic* field change over a well-defined distance L is thus a perfect tool to reorient the polarization with respect to the guide field.[36] Devices doing this are called neutron *spin flippers* (see Fig 3.19). They are a vital component of any spin-echo spectrometer. The most common flippers change the polarization by 90° or 180° with respect to the guide field. They are called $\pi/2$ and π flippers, respectively.

The ratio of the Larmor frequency over the angular frequency of the field change as seen in the neutron's frame of reference

$$C = \omega_L \Big/ \frac{\mathrm{d}\theta_B}{\mathrm{d}t} = -\gamma_L B \Big/ \frac{\mathrm{d}\theta_B}{\mathrm{d}z} v \tag{3.104}$$

determines whether a field change may be considered adiabatic or not. An adiabadicity parameter of $C = 10$ implies that the polarization of the beam precesses 10 times before the guide field $\vec{B}$ has completed a full turn. For a beam centered on

[35] There is a whole area of neutron scattering devoted to creating stable polarized beams in field-free regions generated either via super-conducting (cryo-pad) or $\mu - metal$ shielding (μ-pad). We will not further discuss this technique here, but refer to the literature [57].

[36] The rotation angle of the polarization is a function of the time the neutrons spend within the field. It thus depends on the neutron wavelength. Such devices have, therefore, diminishing performance for broad wavelength bands.

a nominal wavelength of 5 Å such a C can be achieved provided the field gradient along $\hat{z}$ does not exceed 0.13 T (or 1.3 kGauss) per cm.[37]

We now will consider in more detail the evolution of the polarization of a beam with a finite component perpendicular to the field ($\vec{P}_\perp \perp \vec{B}$). According to Eq. (3.102) and (3.103) the polarization $\vec{P}_\perp$ will accumulate a precession angle proportional to the field integral

$$\phi = \gamma_\mathrm{L} \int_0^L \frac{1}{v(\vec{l})} \vec{B} \cdot \mathrm{d}\vec{l}. \tag{3.105}$$

In general, the trajectory can be assumed rectilinear and the velocity constant. In addition, we may restrict ourselves without loss of generality to the case where $\vec{P}_\perp = \vec{P}$. This allows describing the precession of the polarization vector by the number N_p of turns it performs about the field axis. N_p is given by the simple expression

$$N_p = \frac{\phi}{2\pi} = 7361 \cdot B[\mathrm{Tesla}] \cdot L[\mathrm{m}] \cdot \lambda[\mathrm{Å}], \tag{3.106}$$

where L denotes the length of the trajectory in the field region. For a field of 0.1 T and 5 Å neutrons, this amounts to 3680 turns per meter. A neutron with a different velocity will acquire a different phase angle. Thus a distribution in the neutron velocity will lead quickly to a complete smearing of the polarization because

$$\vec{P} = \int \mathrm{d}^3k \; p(\vec{k}) \, \vec{P}(\phi(\vec{k})) = 0, \tag{3.107}$$

if the orientation of the polarization vectors given by the precession angle

$$\phi(\vec{k}) = \frac{\gamma_\mathrm{L} m}{\hbar k} \int_0^L \vec{B} \cdot \mathrm{d}\vec{l} \tag{3.108}$$

is distributed randomly over 2π. This would mean that we have missed our goal of increasing the intensity by accepting a broad wavelength band for the measurement. Fortunately, a loss of beam polarization does not mean a loss of quantum coherence of single neutrons. To the contrary, as the neutrons do not encounter statistical perturbations along their trajectories, the quantum state of any single neutron is at

[37] To get an idea about field strength: The earth magnetic field has a strength of about 0.5 Gauss, which is equivalent to 0.05 mT. A strong permanent neodymium magnet ($Nd_2Fe_{14}B$) used in hard-disk drives can reach values above 1 T, and strong superconducting laboratory magnets achieve nearly 20 T in continuous operation. The highest magnetic fields ($B > 10^8$) Tesla that are observed in the universe stem from neutron stars. The question of whether in these stars the magnetic field could move only with the charged particles, leaving the neutrons behind, is a matter of current scientific debate.

any time fully correlated with its state at $t = 0$, that is, at the point of entry into the precession region.[38] It is thus in principle possible to restore the polarization of the beam even for a distribution of wavelengths. The practical realization of such a polarization restoration is called *spin echo*. According to Eq. (3.102) the polarization $\vec{P}$, its variation as a function of time $\mathrm{d}\vec{P}/\mathrm{d}t$ and the field $\vec{B}$ form a right-handed orthogonal system (remember that γ_L is negative). The precession angle in the laboratory frame thus changes sign upon reversal of either the field or the polarization direction. Therefore, if we can identify a point L' along the trajectory such that for all neutrons

$$\int_0^{L'} \vec{B} \cdot \mathrm{d}\vec{l} = \int_{L'}^{L} \vec{B} \cdot \mathrm{d}\vec{l}, \tag{3.109}$$

then by flipping $\vec{P}$ by 180° at L' we will obtain a full echo of the polarization at L

$$\vec{P}(L) = \vec{P}(0). \tag{3.110}$$

Practically, the echo can be achieved with a beam traveling down two magnetic coils of identical characteristics with a π-flipper in between (see Fig. 3.20).[39]

The spin-echo set-up becomes a neutron spectrometer[40] by (i) placing a sample[41] after the π-flipper and (ii) analyzing the component of the final polarization $\vec{P}_f$ along its initial value $\vec{P}_i$:

$$P = \vec{P}_f \cdot \vec{P}_i = \vec{P}(L) \cdot \vec{P}s(0). \tag{3.111}$$

This so-called *linear polarization analysis* is achieved by flipping the polarization after the second spin-echo coil by $\pi/2$ and passing the beam through a spin analyzer. The intensity I_{Det} measured in the detector is related to P via the expression

$$I_{\mathrm{Det}} = \frac{I_0}{2}(1+ < P >), \tag{3.112}$$

---

[38] For a single neutron $|\vec{P}|$ is preserved. The depolarization of the beam arises from the fact that for every neutron with polarization vector $\vec{P}$ we find another one in the beam with $\vec{P}' = -\vec{P}$.

[39] In principle, one could equally work with two coils with opposite field directions. In practice, one prefers often the version with identical fields and a π-flipper. In that case, the two coils can be put into series assuring identical currents. In addition, opposite field directions would make it more difficult to create homogeneous field components along the trajectory.

[40] In resonance spin-echo spectroscopy, the two precession solenoids are substituted by two pairs of radiofrequency coils. As this does not change the basic principle, we refer the reader to the literature for further insight into this very interesting technique [58].

[41] We assume for the moment that the sample does not alter the polarization of the beam. This is the case for nuclear coherent and isotope incoherent scattering.

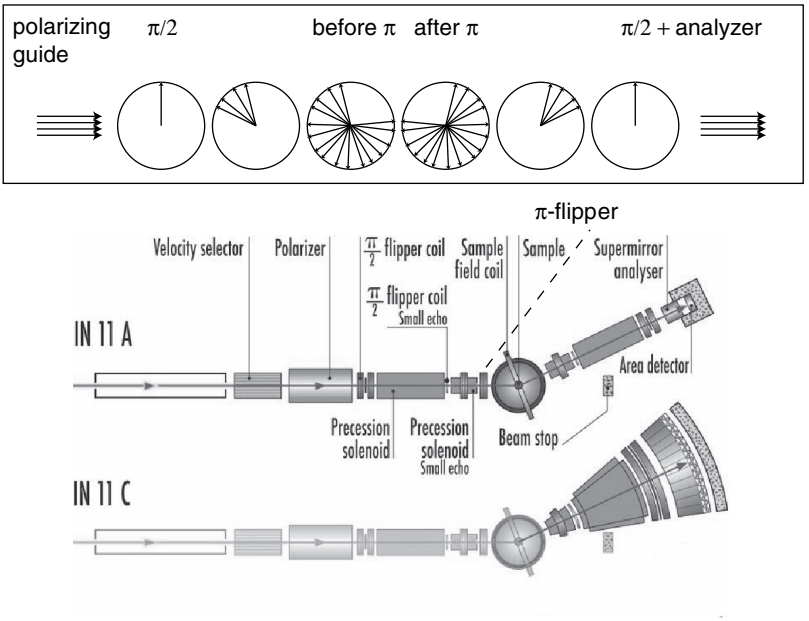

Fig. 3.20 The archetypical spin-echo spectrometer IN11. A guide delivers neutrons from the cold source. The nominal wavelength can be chosen between 3.8 and 12 Å. A velocity selector filers out a 15–22% wide wavelength band. A FeAg suppermirror polarizer creates a beam with 99% polarization parallel to the beam direction. At the entrance of the first precession solenoid, the spin is flipped by $\pi/2$ so that now $\vec{P} \perp \vec{B}$. This flip corresponds to the start of the precession in the first spectrometer arm. Just before the beam reaches the sample, the polarization is reversed by a π turn and the neutrons start precessing in the opposite sense in the second arm of the spectrometer. The polarization is thus restored for elastic scattering provided the field integrals in the two arms are equal. The polarization is flipped back along the beam direction at the end of the second precession solenoid. The projection of the polarization onto the field axis after the $\pi/2$ flip corresponds to the component of the polarization before the $\pi/2$ flip parallel to the initial polarization (see Eq. (3.111)). It is analyzed with the help of a CoTi supermirror. The maximum field integral that can be achieved in this set-up over 2 m is 0.27 T·m. This corresponds according to Eq. (3.126) to a spin-echo time of about 3 ns at 4 Å. When studying relaxations it is important to cover several orders of magnitude in time. For a fixed wavelength this is achieved by varying the field integral. On IN11 very short times, that is, very small field integrals, are produced with a second set-up consisting of shorter solenoids. The reason resides in the fact that it becomes increasingly difficult to have stable spin-echo conditions at very low fields in large coils due to stray fields from the flippers and ultimately the earth magnetic field. Combining the two set-ups it is possible to cover three orders of magnitude in spin-echo time at one wavelength. Field homogeneity is important for the performance of a spin-echo spectrometer. This limits the accessible solid scattering angle that can be covered simultaneously. The IN11C spectrometer offers a $30^\circ \times 1.5^\circ$ solid angle by using a fan-shaped secondary spectrometer. For comparison, the solid angle sustained by IN11A is only $0.9^\circ \times 0.9^\circ$. The larger opening has a certain price in resolution. The maximum spin-echo time measurable with IN11C is only 0.5 ns at 4 Å

where the brackets indicate averaging over all neutrons. I_0 is the mean intensity of the detected beam and as such—within the approximation discussed in Section 3.4.4—proportional to the static structure factor for the scattering vector under consideration:

$$I_0 \propto \int S(\vec{Q}, \hbar\omega)\mathrm{d}\omega \equiv S(\vec{Q}). \tag{3.113}$$

Under the condition that (i) the beam is monochromatic and that (ii) the scattering is elastic we obtain according to Eq. (3.105) a sinusoidal response if we scan the current and thus the field integral in the second arm of the spectrometer.[42]

$$P = \cos\phi = \cos\left(\gamma_L(B_1L_1 - B_2L_2)/v\right) = \cos(\epsilon\lambda) \tag{3.114}$$

with

$$\epsilon = \gamma_L \frac{m(B_1L_1 - B_2L_2)}{h}. \tag{3.115}$$

For a distribution of velocities $p(v)$, the result is a simple superposition of the monochromatic response as long as we stay with elastic scattering

$$P = <\cos\phi> = \int_0^\infty p(v)\cos\left(\gamma_L(B_1L_1 - B_2L_2)/v\right)\mathrm{d}v, \tag{3.116}$$

$$= \int_0^\infty p(\lambda)\cos(\epsilon\lambda)\,\mathrm{d}\lambda. \tag{3.117}$$

This expression, which defines the shape of the spin-echo curve, is simply the Fourier-transform[43] of the wavelength distribution of the beam in terms of the field integral difference expressed via the variable ϵ. For a 10–15% wavelength spread we can expect to observe in the order of 10 oscillations (see Fig. 3.21).

We will now consider the case of inelastic scattering. The velocity of the neutrons changes from v_1 in the first arm to v_2 in the second arm with

$$\hbar\omega = \frac{m}{2}\left(v_2^2 - v_1^2\right). \tag{3.118}$$

For a single scattering channel $v_1 \rightarrow v_2$, the resulting polarization is given by

$$P = \cos\left(\gamma_L\left[\frac{B_1L_1}{v_1} - \frac{B_2L_2}{v_2}\right]\right). \tag{3.119}$$

[42] In practice, this is done by a small extra coil in one of the spectrometer arms.

[43] Strictly speaking, we get the cosine-transform of the wavelength distribution. For symmetric functions the cosine transform is, however, identical to the Fourier transform.

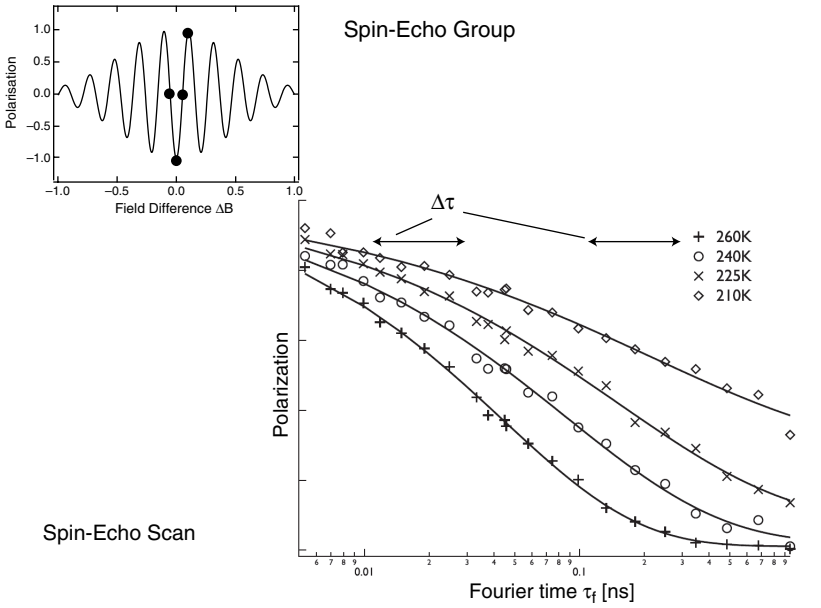

Fig. 3.21 Spin-echo experiment. The aim of a spin-echo experiment is to measure the loss of polarization as a function of the Fourier time τ_f. The fundamental scan parameter is the field integral in the two main precession coils (symmetric scan). For every setting of the spectrometer the various correction fields are tuned such as to produce a maximum spin echo for an elastic scatterer according to Eq. (3.109). The spin echo is determined by applying a small field difference ΔB to one of the spectrometer arms (asymmetric scan). This leads to an oscillating spin-echo response called the spin-echo group. The envelop of this group is the cosine transform of the wavelength distribution of the beam according to Eq. (3.117). In practice, one refrains from measuring the full spin-echo group as this would be too time consuming. Four points as indicated in the figure are sufficient to determine the amplitude and phase of the group with good precision. The spin-echo group delivers the polarization for a particular spectrometer setting. The presence of inelastic processes leads to a drop of the polarization. Relaxation processes become active polarization suppressors as their decay time falls into the window of the spin-echo time. In general, it is sufficient to consider the amplitude of the spin-echo signal. In the example given (the glass-former cis-Decalin measured on the spin-echo spectrometer IN11C at the ILL), the evolution of the polarization amplitude as a function of Fourier time and sample temperature shows that the relaxation time of the liquid becomes longer as the temperature decreases. The spin-echo technique integrates the relaxation function over rather broad time windows Δt (graphics courtesy of P. Fouquet and S. Eibl)

If we are dealing with a distribution of incoming neutrons and a multitude of scattering channels, then

$$P = \int_0^\infty \int_0^\infty p(v_1) T(v_1, v_2) \cos\left(\gamma_L \left[\frac{B_1 L_1}{v_1} - \frac{B_2 L_2}{v_2}\right]\right) \mathrm{d}v_1 \mathrm{d}v_2, \quad (3.120)$$

$$\equiv \int_0^\infty \int_0^\infty p(\lambda_1) T(\lambda_1, \lambda_2) \cos\left(\epsilon_1 \lambda_1 - \epsilon_2 \lambda_2\right) \mathrm{d}\lambda_1 \mathrm{d}\lambda_2, \quad (3.121)$$

with the transfer function $T(v_1, v_2)$ expressing the normalized probability that a neutron of velocity v_1 is scattered into a neutron with velocity v_2. If properly transformed into energy space, then $T(v_1, v_2)$ is nothing else but the scattering function $S(\hbar\omega)$ correctly integrated over the accessible Q-range. Although accurate, the above expression, which could be considered the master equation of spin-echo spectroscopy, does not lend itself easily to a physical interpretation. This holds even if we restrict ourselves to the spin-echo point for elastic scattering ($\epsilon_1 = \epsilon_2 = \gamma_L m B L/h$), in which case the above equation simplifies to

$$P = \int_0^\infty p(\lambda_1)\mathrm{d}\lambda_1 \int_0^\infty T(\lambda_1, \lambda_2)\cos\left(\epsilon_1(\lambda_1 - \lambda_2)\right)\mathrm{d}\lambda_2. \tag{3.122}$$

The situation changes if we restrict ourselves to small energy transfers. In that case we may approximate v_2 by $v_1 + \hbar\omega/m v_1$. This leads for a specific scattering channel to

$$P = \cos\left(\gamma_L\left[\frac{B_1 L_1}{v_1} - \frac{B_2 L_2}{v_1 + \hbar\omega/m v_1}\right]\right), \tag{3.123}$$

which to leading order in $\hbar\omega$ results in

$$P = \cos\left(\gamma_L\left[\frac{B_1 L_1 - B_2 L_2}{v_1} + \frac{B_2 L_2}{m v_1^3}\hbar\omega\right]\right). \tag{3.124}$$

Under the spin-echo condition for purely elastic scattering[44], the first term in the above equation is zero and we are left with

$$P = \cos\left(\gamma_L \frac{B_2 L_2}{m v_1^3}\hbar\omega\right) = \cos\left(\gamma_L \frac{m^2 B_2 L_2}{2\pi h^2}\lambda_0^3\,\omega\right) = \cos(\tau_f \cdot \omega), \tag{3.125}$$

where we have introduced the Fourier time

$$\begin{aligned}\tau_f &= \gamma_L \frac{m^2 B_2 L_2}{2\pi h^2}\lambda_0^3, \\ &= 0.1863\,[\mathrm{ns}]\,(B_2 \cdot L_2)\,[\mathrm{Tesla}\cdot\mathrm{m}]\,\lambda_0^3\,[\mathrm{\AA}^3].\end{aligned} \tag{3.126}$$

Summing over all scattering channels on the basis of Eq. (3.121) we obtain

$$P(\vec{Q}, \tau_f) = <\cos(\omega\tau_f)> = \frac{\int S(\vec{Q}, \hbar\omega)\cos(\omega\tau_f)\mathrm{d}\omega}{\int S(\vec{Q}, \hbar\omega)\mathrm{d}\omega} \equiv \tilde{I}(\vec{Q}, \tau_f). \tag{3.127}$$

[44] We may choose in principle any fixed value for the energy transfer for the spin-echo condition [59]. This is, for example, useful when measuring the width of an excitation with high precision using a combination of spin-echo and three-axis techniques. This is realized at the TRISP instrument at the FRM-II in Munich [60].

Here we have used the fact that for small energy transfers the momentum transfer is well approximated by its elastic value $\vec{Q} \approx k_i(\hat{k}_i - \hat{k}_f)$. The measured polarization $P(\vec{Q}, \tau_f)$ thus corresponds to the Fourier transform of the scattering function[45] normalized to the static structure factor $S(\vec{Q})$. This statement is true under the assumption that the energy integration covers all active fluctuation processes. We have discussed this problem already in Section 3.4.4. The measured polarization thus can be identified with the normalized *intermediate scattering function* $\tilde{I}(\vec{Q}, \tau_f)$. The Fourier time τ_f depends according to Eq. (3.126) linearly on the field integral. The wavelength enters to the third power. To attain large times, that is, slow relaxations, it is thus preferable to work with long wavelengths provided that the scattering triangle (see Section 3.2) for the $\vec{Q}$ to be investigated can be closed. The static structure factor is normally determined by performing a measurement at low temperatures where the inelastic processes are frozen out. If we take as a concrete example the Lorentzian scattering function given by Eq. (3.80), then the intermediate scattering function derived from the polarizability using Eq. (3.127) leads us back to the exponential relaxation of Eq. (3.79).

At this point we have not yet included the averaging over the wavelength distribution of the incoming beam. We have, therefore, not really gained with respect to the spectrometers working in $(\vec{Q}, \hbar\omega)$-space. Incorporating a wavelength spread in the incoming beam leads to the following expression for the polarizability:

$$P(\vec{Q}, \tau_f) = \int p(\lambda)\, \tilde{I}(\vec{Q}, \tau_f(\lambda))\, \mathrm{d}\lambda. \tag{3.128}$$

This integral corresponds effectively to a smearing of the Fourier time τ_f. For a Gaussian distribution of wavelengths centered on the nominal wavelength λ_0,

$$p(\lambda) = \frac{1}{\sqrt{2\pi a^2}} \exp\left(-\frac{(\lambda - \lambda_0)^2}{2a^2}\right), \tag{3.129}$$

we can calculate the mean Fourier time and mean standard deviation as

$$\tau_0 = \int p(\lambda)\, \tau_f(\lambda)\, \mathrm{d}\lambda \approx 1.02\, \tau_f(\lambda_0) \tag{3.130}$$

$$\Delta\tau = \sqrt{\int p(\lambda)\, \tau_f^2(\lambda)\, \mathrm{d}\lambda - \tau_0^2} \approx 0.3\, \tau_0, \tag{3.131}$$

where the numerical values [41] correspond to a typical 15% wavelength band. The mean Fourier time is thus practically not affected by the time smearing. The relative Fourier time uncertainty $\Delta\tau/\tau_0$, however, is rather large and constant for all Fourier times. This is, however, generally not a problem as relaxation processes take place

[45] As outlined before this is true for symmetric functions. As we are, however, interested in small energy transfers, $S(\vec{Q}, \hbar\omega)$ is symmetric for all but the lowest temperatures.

on exponential scale and thus do not vary rapidly with time. The important feature of spin echo is not the time resolution but the dynamic range in particular toward very long times. Using strong solenoids in conjunction with short wavelengths, it is currently possible to attain Fourier times close to 0.5 µs. According to Eq. (3.82) this translates into an energy of 1 neV. It is completely unthinkable to obtain such a resolution for a classical scattering experiment in $(\vec{Q}, \hbar\omega)$-space by tailoring the distribution functions of the beam. We would be obliged to sacrifice for identical detector solid angle four to five orders of magnitude in flux.

So far we have treated the spin-echo instrument as ideal. In the real world we have to live with imperfections. Among these we find, for example, variations of the field integral as a function of the neutron trajectory. These variations are the more important the more divergent the beam. They can be corrected for by using special Fresnel coils [61]. Despite all these efforts fields and trajectories will never be ideal. It is thus important to measure the resolution as a function of Fourier time. The best candidate is the sample itself at it has exactly the same geometry and thus will produce the right beam dimensions and divergences after the scattering. To freeze out the slow motions the resolution measurement has to be done at low temperatures. Under these elastic conditions any drop in polarization $P_{\text{elastic}}(Q, \tau_f)$ must be attributed to instrumental imperfections. The physical signal must be taken with respect to this baseline. The corrected polarization arising from the sample $P_S(Q, \tau_f)$ is thus given by

$$P_S(Q, \tau_f) = \frac{P_{\text{measured}}(Q, \tau_f)}{P_{\text{elastic}}(Q, \tau_f)}. \tag{3.132}$$

Contrary to spectrometers operating in energy space, the process of resolution correction is thus not a complex de-convolution but a simple division. In most cases it is the resolution and not the technically achievable field integrals that limits the maximum Fourier times. We usually consider that this limit has been achieved when the polarization $P_{\text{elastic}}(Q, \tau_f)$ has dropped to a value of $1/e$.

When deriving the spin-echo relations we have tacitly assumed that the spin of the neutrons is not affected by the scattering process. This is strictly true only for coherent and isotope incoherent nuclear scattering. In the case of spin incoherent scattering, two-third of the events lead to a spin flip irrespective of the precise scattering geometry. These neutrons will not restore their original polarization traveling down the secondary spectrometer. Therefore, in a general experiment with the π-flipper active the polarization measured at any Fourier time will correspond to

$$P_{\text{measured}}(Q, \tau_f) = P_{\text{coh}} \frac{I_{\text{coh}}}{I_{\text{coh}} + I_{\text{inc}}}(Q, \tau_f) - \frac{1}{3} P_{\text{inc}} \frac{I_{\text{inc}}}{I_{\text{coh}} + I_{\text{inc}}}(Q, \tau_f), \tag{3.133}$$

where $\vec{P}_{\text{coh}}$ and $\vec{P}_{\text{inc}}$ denote the values for the polarization that one would obtain from hypothetical samples of purely coherent or incoherent character, respectively. The normalization of this function is no longer trivial as the coherent (collective) and incoherent (single particle) dynamic response of the sample will not necessarily

take place on the same time scale. Therefore, the ratios of scattering intensities $I_{\mathrm{coh}}/I_{\mathrm{coh}} + I_{\mathrm{inc}}$ and $I_{\mathrm{inc}}/I_{\mathrm{coh}} + I_{\mathrm{inc}}$ are functions of $\vec{Q}$ and τ_f. The situation becomes even more complex in the case of magnetic scattering. For a paramagnetic sample the magnetic scattering can take over the role of a π-flipper of proper orientation, that is, it turns the polarization by 180° about a well-defined axis. In consequence, by doing a measurement with and without a π-flipper, it is possible to separate the dynamic paramagnetic from the coherent and isotope incoherent nuclear response. The investigation of ferro-magnetic samples is possible under certain conditions, but the discussion of these techniques is beyond the scope of this introduction.

The requirement of very precise field integrals makes it difficult to achieve very large solid angles with the conventional spin-echo technique. This is a real drawback, for example, compared to backscattering spectrometers with very large analyzers. The problem can be alleviated for medium-resolution spin-echo spectrometers by using a spherically symmetric design. This principle was successfully implemented with the SPAN [62, 63] spectrometer at the Hahn Meitner Institut in Berlin, Germany. A similar project called WASP [64] is part of the instrument upgrade program at the Institut Laue Langevin in Grenoble, France.

If the beam is pulsed, then it is a priori possible to combine time-of-flight with the spin-echo technique [65]. For slow processes the neutrons arriving in the detector as a function of time can be characterized according to their wavelength. The measured polarization as a function of time thus pertains to a wavelength band, the width of which can be controlled via the time structure of the beam. The technical challenge of time-of-flight spin echo resides in the fact that the fields in the solenoids as well as in the flippers and other correction elements have to follow the evolution of the wavelength as a function of time. This has, however, been demonstrated technically feasible [65]. The advantages of such a technique are obvious in the case of a pulsed source. Time-of-flight spin-echo spectroscopy can, however, equally be of great interest at continuous sources, in particular when the signal to be measured is spread over a large dynamic range.

3.5 Concluding Remark

It cannot be the aim of this introduction to neutron instrumentation to be comprehensive. There are many other important aspects, such as polarization analysis [56] or Laue diffraction [66], that have not even been touched upon. Imaging techniques will be dealt with in another book in this series. In all cases there is a large amount of literature that deals specifically with these concepts.

Acknowledgments I would like to thank Ken Andersen, Bob Cubitt, Charles Dewhurst, Björn Fåk, Henry Fischer, Peter Fouquet, Bernhard Frick, Arno Hiess, and Jacques Ollivier for a critical reading of the manuscript and Hannu Mutka for clarifying questions involving 2π. I would like to present my apologies to Anita, Carmen, Rafaëla, and Alexander for the evenings and weekends spent in front of the computer instead of having had fun with them.

References

1. J. Chadwick, Nature **129**, 312 (1932).
2. J. Chadwick, Proc. Roy. Soc. A **136**, 692 (1932).
3. *Neutron Data Booklet*, A-J. Dianoux and G. Lander (Eds.), Institut Laue-Langevin, Grenoble, France (2002).
4. A. Taylor et al., Science **315**, 1092 (2007).
5. J.M. Carpenter and W.B. Yelon, *Neutron Sources*, in *Neutron Scattering*, K. Sköld and D.L. Price (Eds.) *Methods of Experimental Physics* **23** A, Academic Press, New York (1986).
6. P.A. Kopetka, J.M. Rowe, and R.E. Williams, *Cold Neutrons at NIST*, Nuclear Engineering and Technology **38**, 427 (2006).
7. P. Ageron, Nuclear Instr. and Meth. A **284**, 197 (1989).
8. F. Mezei, J. Neutron Res. **6**, 3 (1997).
9. The ESS Project, Volume I-IV, Jülich, Germany (2002).
10. H. Maier-Leibnitz, Nukleonik **2**, 5 (1966).
11. H. Rauch and S. Werner, *Neutron Interferometry*, Oxford University Press, Oxford (2000).
12. B. Dorner, J. Neutron Res **13**, 267 (2005).
13. G.L. Squires, *Introduction to the Theory of Thermal Neutron Scattering*, Cambridge University Press, Cambridge (1978).
14. S.W. Lovesey, *Theory of Neutron Scattering from Condensed Matter*, Vol. 1: *Nuclear Scattering*, Vol. 2: *Polarization Effects and Magnetic Scattering*, Oxford University Press, Oxford (1984).
15. D.L. Price and K. Sköld, in *Neutron Scattering*, K. Sköld and D.L. Price (Eds.) *Methods of Experimental Physics* **23** A, Academic Press, New York (1986).
16. B. Dorner, Acta Cryst. A **28**, 319 (1972).
17. J. Felber, R. Gähler, R. Golub, and K. Prechtl, Physica B **252**, 34 (1998)
18. H. Schober, E. Farhi, , F. Mezei, P. Allenspach, K. Andersen, P.M. Bentley, P. Christiansen, B. Cubitt, R.K. Heenan, J. Kulda, P. Langan, K. Lefmann, K. Lieutenant, M. Monkenbusch, P. Willendrup, J. Saroun, P. Tindemans, and G. Zsigmond, Nuclear Instr. Methods A **589**, 34 (2008).
19. E. Fermi and W.H. Zinn, Phys. Rev. **70**, 103 (1946).
20. L. Dobrzynski, K. Blinowski, and M. Cooper, *Neutrons and Solid State Physics*, Ellis Horwood, New York, London, Toronto, Sydney, Tokyo, Singapore (1994).
21. A.I. Frank, Sov. Phys. Usp. **25**, 280 (1982).
22. C. Schanzer, P. Böni, U. Filges, and T. Hils, Nuclear Instr. Methods A **529**, 63 (2004).
23. D.P. Mitchell and P.N. Powers, Phys. Rev. **50**, 486 (1936).
24. W.H. Zinn, Phys. Rev. **71**, 752 (1947).
25. R. Currat, *Three-Axis Inelastic Neutron Scattering*, in *Neutron and X-ray Spectroscopy*, F. Hippert, E. Geissler, J.L. Hodeau, E. Lelièvre-Berna, and J.R. Regnard (Eds.), Springer, Grenoble (2006).
26. A. Magerl and V. Wagner (Eds.) *Focusing Bragg Optics*, Nuclear Instr. Methods A, **338**, 1-152 (1994).
27. RE. Lechner, R.v. Wallach, H.A. Graf, F.-J. Kasper, and L. Mokrani, Nuclear Instr. Meth A, **338**, 65 (1994).
28. V.F. Sears, *Neutron Optics*, Oxford University Press, New York (1989).
29. C.G. Darwin, Phil. Mag. **27**, 315, 675 (1914).
30. E. Fermi, J. Marshall, and L. Marshall, Phys. Rev. **72**, 193 (1947).
31. N. Holt, Rev. Sci. Instrum. **28**, 1 (1957).
32. H. Friedrich, V. Wagner, and P. Wille, Physica B, **156**, 547 (1989).
33. L. Dohmen, J. Thielen, and B. Ahlefeld, J. Neutron Res **13**, 275 (2005).
34. C.D. Clark, E.W. Mitchell, D.W. Palmer, and I.H. Wilson, J. Sci. Instrum. **43**, 1 (1966).
35. M. Kempa, B. Janousova, J. Sarouna, P. Flores, M. Böhm, F. Demmel, and J. Kulda, Physica B, **385-386** 1080 (2006).

36. M.J. Cooper and R. Nathans, Acta Cryst. **23**, 357 (1967).
37. A.K. Freund, Nuclear Instr. Methods **213**, 495 (1983).
38. B. Frick, *Neutron Backscattering Spectroscopy*, in *Neutron and X-ray Spectroscopy*, F. Hippert, E. Geissler, J.L. Hodeau, E. Lelièvre-Berna, and J.R. Regnard (Eds.), Springer, Grenoble (2006).
39. H. Mutka, Nuclear Instr. Methods A, **338**, 145 (1994).
40. R.E. Lechner, Proc. Workshop on Neutron Scattering Instrumentation for SNQ, Maria Laach, Sept. 3–5, 1984; R. Scherm and H. Stiller (Eds.), Jül-1954, p. 202 (1984).
41. R.E. Lechner and S. Longeville, *Quasielastic Neutron Scattering in Biology, Part I: Methods* in Neutron Scattering in Biology, Techniques and Applications, J. Fitter, T. Gutberlet, and J. Katsaras, (Eds.), Springer Verlag, Berlin (2006), pp. 309–354.
42. K. Lefmann, H. Schober, and F. Mezei, Meas. Sci. Technol. **19**, 034025 (2008).
43. G.E. Bacon, *Neutron Diffraction* 3rd edn., Clarendon, Oxford (1975).
44. H.E. Fischer, A.C. Barnes, and P.S. Salmon, Rep. Prog. Phys. **69**, 233 (2006).
45. W. Schäfer, Eur. J. Mineral. **14**, 263 (2002).
46. A.W. Hewat, Nuclear Instr. Methods **127**, 361 (1975).
47. C.G. Windsor, *Pulsed Neutron Scattering*, Taylor and Francis, London (1981).
48. K. Lieutenant, T. Gutberlet, A. Wiedenmann, and F. Mezei, Nuclear Instr. Methods A **553**, 592 (2005).
49. S.K. Sinha, E.B. Sirota, S. Garoff, and H.B. Stanley, Phys. Rev. B **38**, 2297 (1988).
50. J. Daillant and A. Gibaud *X-ray and Neutron Reflectivity: Principles and Applications*, Springer Verlag , Berlin (1999).
51. V. Lauter-Pasyuk, H.J. Lauter, B.P. Toperverg, L. Romashev, and V. Ustinov, Phys. Rev. Lett. **89** 167203 (2002).
52. F. Mezei, Z. Physik **255**, 146 (1972).
53. F. Mezei, *The Principles of Neutron Spin Echo* in *Neutron Spin Echo*, Lecture Notes in Physics, Vol. 128, Ed. F. Mezei, Springer Verlag, Berlin (1980).
54. F. Mezei, *Fundamentals of Neutron Spin Echo Spectroscopy* in *Neutron Spin Echo Spectroscopyy, Basics, Trends and Applications*, F. Mezei, C. Pappas, and T. Gutberlet (Eds.), Springer Verlag, Berlin, Heidelberg, New York (2003).
55. R. Cywinski, *Neutron Spin Echo Spectroscopy*, in *Neutron and X-ray Spectroscopy*, F. Hippert, E. Geissler, J.L. Hodeau, E. Lelièvre-Berna, and J.R. Regnard (Eds.), Springer, Berlin (2006).
56. W.G. Williams, *Polarized Neutrons*, Clarendon, Oxford (1988).
57. E. Lelievre-Berna, P.J. Brown, F. Tasset, K. Kakurai, M. Takeda, L.-P. Regnault, Physica B **397**, 120 (2007).
58. M. Bleuel, F. Demmel, R. Gähler, R. Golub, K. Habicht, T. Keller, S. Klimko, I. Köper, S. Longeville, and S. Prodkudaylo, *Future Developments in Resonance Spin Echo* in *Neutron Spin Echo Spectroscopyy, Basics, Trends and Applications*, F. Mezei, C. Pappas, and T. Gutberlet (Eds.), Springer Verlag, Berlin, Heidelberg, New York (2003).
59. K. Habicht, R. Golub, R. Gähler, and T. Keller, *Space-Time View of Neutron Spin-echo, Correlation Functions and Phonon Focusing* in *Neutron Spin Echo Spectroscopyy, Basics, Trends and Applications*, F. Mezei, C. Pappas, and T. Gutberlet (Eds.), Springer Verlag, Berlin, Heidelberg, New York (2003).
60. T. Keller, K. Habicht, H. Klann, M. Ohl, H. Schneider, and B. Keimer, Appl. Phys. A **74** [Suppl.], S332 (2002).
61. T. Keller, R. Golub, F. Mezei, and R. Gähler, Physica B **241**, 101 (1997) and references therein.
62. C. Pappas, G. Kali, T. Krist, P. Böni, and F. Mezei, Physica B **283**, 365 (2000)
63. C. Pappas, A. Triolo, F. Mezei, R. Kischnik, and G. Kali, *Wide Angle Neutron Spin Echo and Time-of-Flight Spectrometer* in *Neutron Spin Echo Spectroscopyy, Basics, Trends and Applications*, F. Mezei, C. Pappas, and T. Gutberlet (Eds.), Springer Verlag, Berlin, Heidelberg, New York (2003).

64. R. Hölzel, P.M. Bentley, and P. Fouquet, Rev. Sci. Instrum. **77**, 105107 (2006).
65. B. Farago, *Time-of-Flight Neutron Spin Echo: Present Status* in *Neutron Spin Echo Spectroscopyy, Basics, Trends and Applications*, F. Mezei, C. Pappas, and T. Gutberlet (Eds.), Springer Verlag, Berlin, Heidelberg, New York (2003).
66. C.C. Wilson and D.A. Myles, *Single Crystal Neutron Diffraction and Protein Crystallography* in Neutron Scattering in Biology, Techniques and Applications, J. Fitter, T. Gutberlet, and J. Katsaras, (Eds.), Springer Verlag, Berlin (2006), pp. 21–42.

http://www.springer.com/978-0-387-09415-1

Neutron Applications in Earth, Energy and Environmental Sciences

Liyuan, L.; Rinaldi, R.; Schober, H. (Eds.)

2009, XVIII, 638 p. 35 illus., Hardcover
ISBN: 978-0-387-09415-1